Tectonics

Interactions between propagating rotational rifts and linear rheological heterogeneities: Insights from three-dimensional laboratory experiments

N. E. Molnar[1] (ID), A. R. Cruden[1] (ID), and P. G. Betts[1] (ID)

[1]School of Earth, Atmosphere and Environment, Monash University, Clayton, Victoria, Australia

Abstract The lateral propagation of rifts is a consequence of the relative divergence of lithospheric plates about a pole of rotation. Modern and ancient examples of rifts are known to overprint preexisting linear anisotropies in the crust and lithosphere, such as lithospheric boundaries, crustal sutures, and thermal anomalies. Here we investigate how propagating rifts interact with preexisting structures by using three-dimensional analogue experiments with rotational extensional boundary conditions and variably oriented linear weak zones in the lithospheric mantle. When linear weaknesses are oriented at low angles to the rift axis, early strain localization occurs in narrow domains, which merge at later stages, resulting in continental breakup by unzipping. Strong strain partitioning is observed when the linear heterogeneity is oriented at high angles with respect to the rift axis. In these experiments, early subparallel V-shaped basins propagate toward the pole of rotation until they are abandoned and strain is transferred entirely to structures developed in the vicinity of the strongly oblique weak lithosphere zone boundary. The experimental results are characterized in terms of their evolution, patterns of strain localization, and surface topography as a function of the lithospheric heterogeneity obliquity angle. Comparison of the experiments to ancient and modern examples in nature may help to elucidate the common but still poorly understood process of propagating rift-lithospheric heterogeneity interaction.

1. Introduction

The orientation of newly formed ocean basin systems often occurs at oblique angles to preexisting continental lithospheric structures such as suture zones, thermal weaknesses, and steps in the base of the lithosphere and Moho. Consequently, ancient orogenic systems and associated boundaries are preserved within the continental lithosphere on opposite sides of oceans. In modern rift systems such as those developed in the East African Rift and the juvenile Red Sea ocean basin, the axis of extension is oriented along the Mozambique Ocean suture zone [*Kazmin et al.*, 1978], oblique to ancient Neoproterozoic sutures [e.g., *Dixon et al.*, 1987] and thermal anomalies associated with mantle convection [e.g., *Chang et al.*, 2011]. Consequently, early held views of the Wilson cycle where continental breakup follows former sutures [*Wilson*, 1966] are not always valid; other compositional and/or thermal weaknesses play an important role in the localization of strain and rifting [e.g., *Corti et al.*, 2003; *van Wijk*, 2005; *Brune*, 2014; *Huismans and Beaumont*, 2014; *Manatschal et al.*, 2015]. Despite their importance for continental rifting and ocean initiation, how preexisting structures or rheological heterogeneities influence the localization and partitioning of deformation during continental breakup remains poorly understood.

The kinematic history of divergent tectonic boundaries is likely to be characterized by multiple phases of successive orthogonal, oblique, and rotational relative motions [e.g., *Bonini et al.*, 1997; *Keep and McClay*, 1997; *Seton et al.*, 2012; *Müller et al.*, 2016]. When lithospheric extension is governed by a rotational component, rift propagation is driven by relative plate motion about a pole of rotation [*Hey et al.*, 1980; *Martin*, 1984]. Simple crustal scale analogue experiments of rotational extension with a homogeneous crust have shown a characteristic triangular fault pattern and rotated blocks comparable to features observed in the Afar triangle [*Souriot and Brun*, 1992]. This paper builds on this research by using analogue experiments to explore how linear lithospheric-scale weak zones interact with propagating rifts during rotational extension, and how this interaction influences deformation and surface topography along the rift axis. Examples of mantle heterogeneities that may be represented in the experiments include active mantle plumes or hot spots [e.g., *Hill*, 1991], mantle penetrating shear zones characterized by reduced grain size [*Bercovici and Ricard*, 2014; *Heron et al.*, 2016], or inherited mechanical anisotropies with lattice preferred orientation of olivine

crystals [*Tommasi and Vauchez*, 2001]. Our experiments also assess the roles propagating rift and lithospheric heterogeneity interactions may have during the transition from continental break up to ocean initiation, the onset of mantle exhumation, and as precursors to transform faults and ridge jumps.

Rift propagation has been the focus of many studies [e.g., *Shih and Molnar*, 1975; *Hey*, 1977; *Courtillot*, 1982; *Martin*, 1984; *Mart and Dauteuil*, 2000; *Hey et al.*, 2010], but few have adopted a quantitative approach to address how continental break up is affected by heterogeneities in the continental lithosphere under rotational boundary conditions [e.g., *Courtillot*, 1982; *Martin*, 1984]. Previous analogue models of oblique rifting [e.g., *Tron and Brun*, 1991; *Mart and Dauteuil*, 2000; *Ding and Li*, 2016] and thermomechanical numerical experiments [*Dunbar and Sawyer*, 1996; *Van Wijk and Blackman*, 2005] successfully investigated the dynamics and mechanics of propagating rifts in three-dimensions under a constant extension direction. Earlier analogue models with an imposed rotational boundary condition focused on specific cases, including the sinistral rotation of the Danakil Block [*Souriot and Brun*, 1992], propagation of rifting from oceanic to continental lithosphere with application to the Havre Trough [*Benes and Scott*, 1996], anticlockwise rollback of the subducting Pacific plate in the Kuril Basin [*Schellart et al.*, 2003], and the opening of the South China Sea [*Sun et al.*, 2009]. In this study we report the first series of three-dimensional, isostatically supported, brittle-ductile multilayer analogue experiments of rotational rifting in order to explore the effect of linear heterogeneities on divergent tectonic boundaries with a rotational component. Specifically, we characterize in detail how deformation propagates and how surface topography evolves within the model lithosphere as a function of the orientation of linear weak zones.

We compare our lithospheric-scale experimental results with natural examples from the Tyrrhenian Sea and the Red Sea-Gulf of Aden rift system, as it represents the best modern example of continental lithosphere that has undergone a transition from rifting to seafloor spreading [*Bosworth et al.*, 2005; *Almalki et al.*, 2015]. The system is not only underlain by a narrow zone of warm upper mantle related to the northward channeling of the Afar plume [*Ritsema et al.*, 1999; *Chang et al.*, 2011; *Hansen and Nyblade*, 2013] but also undergoing a strong rotational relative motion [*Bellahsen et al.*, 2003; *Bosworth et al.*, 2005; *ArRajehi et al.*, 2010] (Figure 1).

2. Experimental Methods and Materials

2.1. Experimental Design

Our experiments focus on the kinematics and mechanics of rifting by attaching a model lithospheric plate to a moving wall pulled by a linear actuator (see section 2.3). In this way, we impose a rotational extensional boundary condition (Figure 2a) that simulates progressive anticlockwise rotation similar to that of natural examples (e.g., Arabian Plate with respect to the African Plate over the last ~13 Ma) [*ArRajehi et al.*, 2010; *Bosworth et al.*, 2005]. Since our apparatus is isothermal, we simulate the presence of linear thermal anomalies by varying the viscosity of the model lithospheric mantle. Although weak zones may not be linear in nature, the model weak zone is analogous to a strain corridor or thermal anomaly with a roughly linear trend. Using this approach, rift-related deformation in the experiments propagates toward a fixed pole of rotation over time, and the propagation path and pattern of strain localization is influenced by the presence and orientation of a linear weakness zone in the mantle lithosphere [e.g., *Agostini et al.*, 2009].

All experiments described here consist of a $44 \times 44 \times 3$ cm three-layer, brittle-ductile model lithospheric plate that floats isostatically on a fluid model asthenosphere contained within a $65 \times 65 \times 20$ cm acrylic tank (Figure 2). Below, we first describe the materials and scaling principles used for the experiments. We then provide details on the experimental apparatus and model construction and finally discuss how deformation and surface topography are monitored during the experiments.

2.2. Materials and Scaling

Lengths, time, and forces are scaled down in analogue experiments in order to produce an appropriately sized model that behaves in a mechanically similar way to nature, over an appropriate period of time [*Ramberg*, 1967; *Davy and Cobbold*, 1991; *Benes and Davy*, 1996]. The experiments reported here comprise a simplified three-layer lithosphere with a brittle upper crust, a ductile lower crust, and a ductile lithospheric mantle, overlying the model asthenosphere (Figure 3a).

The length scale ratio, L^*, for all experiments was fixed by setting the model crustal thickness, $L_m = 14$ mm to represent a crustal thickness in nature $L_p = 35$ km, such that $L^* = L_m/L_p = 4 \times 10^{-7}$, where subscripts m and p
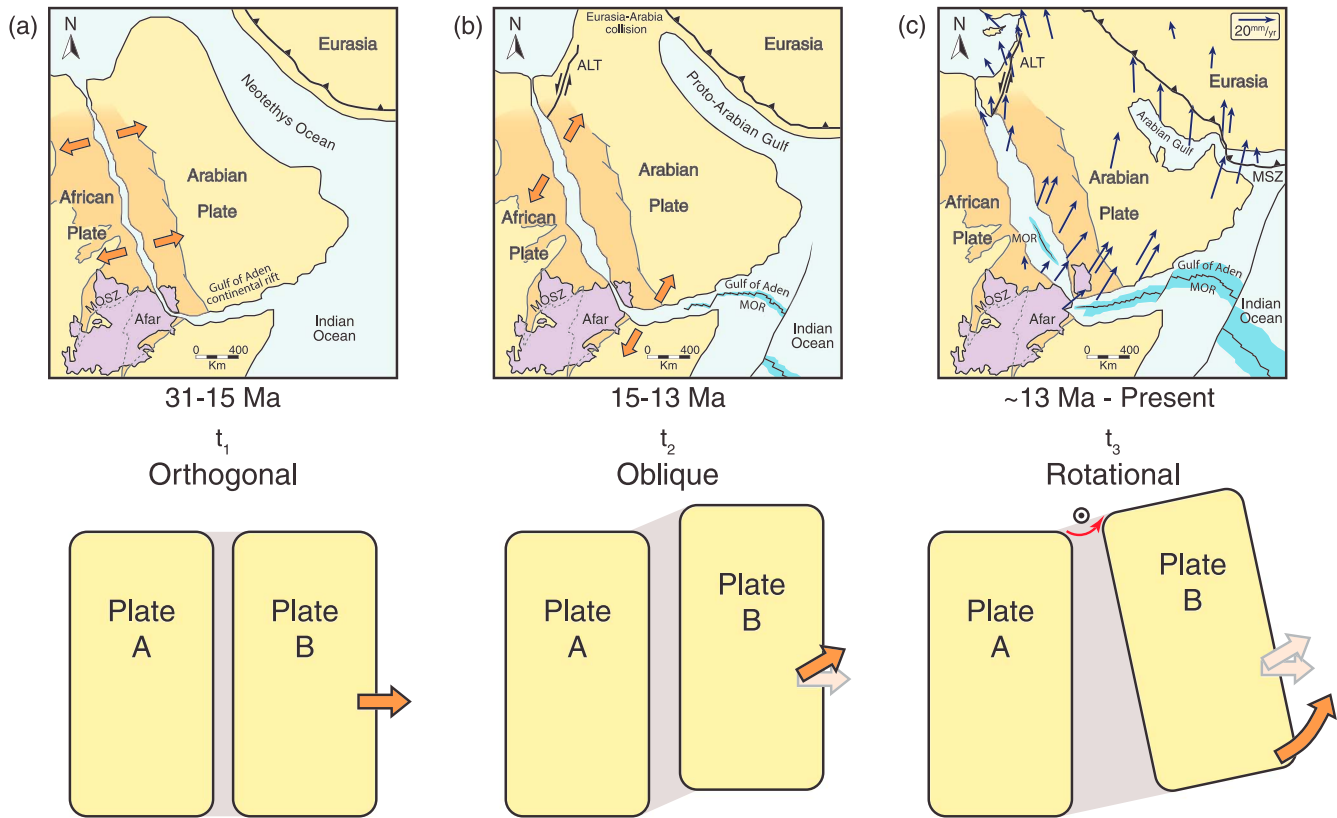
Figure 1. Cartoon reconstruction of the Red Sea-Gulf of Aden rift system Cenozoic evolution summarized in three stages, after *Bosworth et al.* [2005]: (a) Early Oligocene-Middle Miocene: Afar plume initiation and coeval opening of the Red Sea with extension direction normal to the rift axis (N60°E) driven by the closure of the Neotethys Ocean. Mozambique Ocean suture zone (MOSZ) mapped in orange after *Kazmin et al.* [1978]; (b) Middle Miocene-Late Miocene: collision of Arabia with Eurasia led to the formation of the Aqaba-Levant transform (ALT) boundary and the extension direction switched to highly oblique (N15°E) with respect to the Red Sea rift axis. Mid-ocean ridge (MOR) propagated west in the Gulf of Aden. (c) Late Miocene-Present: continent-continent collision to the NW in contrast with the Makran subduction zone (MSZ) in the SE caused a slab pull gradient that resulted in a rotational anticlockwise motion of Arabia with respect to Eurasia. Seafloor spreading in southern Red Sea initiated ~5 Ma. Dark blue arrows represent present-day GPS vectors for Arabia with respect to Eurasia [*ArRajehi et al.*, 2010]. Bottom cartoons illustrate a simplified analogous relative motion of plates. Our laboratory experiments aim to simulate similar boundary conditions to Figure 1c.

refer to the model and natural prototype, respectively. This length scale ratio was suitable for the simulation of large areas on Earth (1100 km × 1100 km) undergoing rotational extension within the confines of our acrylic tank.

Polydimethylsiloxane (PDMS) was used to model the ductile lower crust (Figure 3). PDMS is an optically clear, high viscosity, high molecular weight silicone polymer frequently used in analogue modeling [e.g., *Pysklywec and Cruden*, 2004; *Cruden et al.*, 2006; *Marques et al.*, 2007]. It has density $\rho_m \approx 970$ kg/m^3, which for a natural lower crust density of $\rho_p \approx 2760$ kg/m^3 sets a density scaling factor $\rho^* = \rho_m/\rho_p = 0.355$. PDMS and PDMS mixtures with granular materials have a slightly non-Newtonian rheology defined by the power law:

$$\sigma^n = \eta\dot{\varepsilon} \tag{1}$$

where σ is stress, $\dot{\varepsilon}$ is strain rate, η is viscosity, and n is the power law exponent of the material.

Our PDMS (Wacker Elastomer NA) is a Newtonian viscous fluid with a power law exponent of $n \sim 1$ at our experimental strain rates (1×10^{-5} to 5×10^{-4} s^{-1}). This PDMS has a viscosity of $\eta_m \approx 4 \times 10^4$ Pa s, and if we assume, for scaling purposes, a natural lower crust viscosity of $\eta_n \approx 2 \times 10^{21}$ Pa s, we set a viscosity scaling factor of $\eta^* = \eta_m/\eta_p = 2 \times 10^{-17}$. All experiments were carried out in the normal field of gravity (1 g), so the scale ratio for gravitational acceleration is $g^* = g_m/g_p = 1$. The time scaling factor for the experiments can then be defined as $t^* = \eta^*/\rho^* g^* L^* = t_m/t_p = 1.41 \times 10^{-10}$, meaning that 1 h in the experiment corresponds to ~0.8 Ma in nature. The scaling parameters and experimental and natural material properties and dimensions are summarized in Table 1.
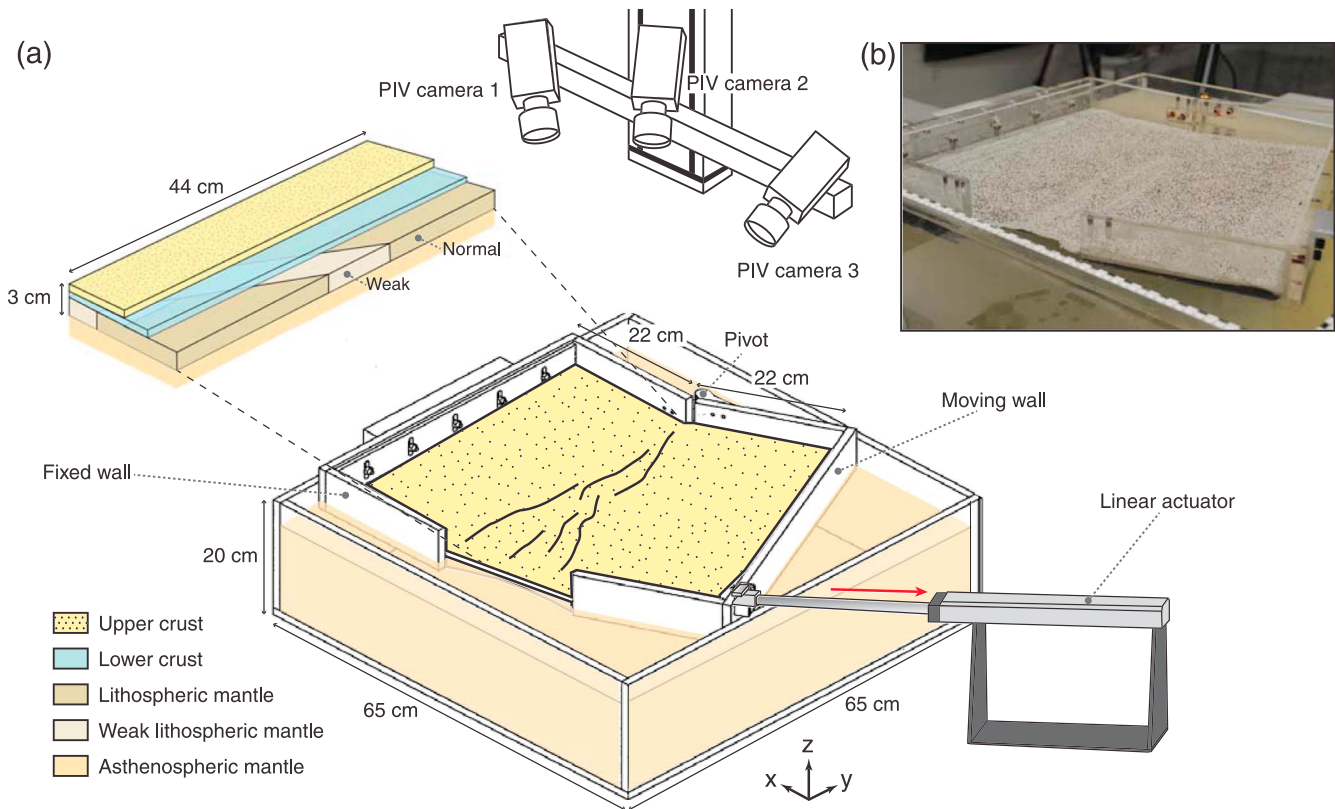
Figure 2. Experimental setup. (a) A 3-D sketch of how the laboratory experiments were constructed. Particle-imaging velocimetry (PIV) cameras 1 and 3 were fixed in a stereoscopic setup to monitor deformation of the model surface. PIV camera 2 captured top-view images with oblique lightening to improve visualization of deformation patterns. (b) Oblique view photo of the analogue model (Experiment 8 after 30% extension).

A solution of Natrosol® 250 HH and sodium chloride in deionized water was used to model the asthenospheric mantle [*Boutelier et al.*, 2016] (Figure 3). Natrosol® is a cellulose-based polymer designed to increase the viscosity of aqueous fluids without significantly affecting their density. As an aqueous solution, it behaves as a Newtonian viscous fluid under conditions typically employed in experimental tectonics [*Boutelier et al.*, 2016].

Considering our scaling factors and the range of values that have been estimated for the viscosity of the asthenosphere in nature ($\sim 10^{19}$ to 10^{20} Pa s [*Artyushkov*, 1983]; $\sim 10^{19}$ to 10^{21} Pa s [*Ranalli*, 1995]), we varied the concentrations of Natrosol® 250 HH [e.g., *Boutelier et al.*, 2016] and sodium chloride [e.g., *Davaille*, 1999; *Davaille et al.*, 2002] to achieve appropriate values for our experiments. The final model asthenosphere has a viscosity of $\eta_m \approx 380$ Pa s, which represents $\eta_p \approx 1.9 \times 10^{19}$ in nature, and has a density of $\rho_m \approx 1100$ kg/m^3, equivalent to a natural asthenosphere density of $\rho_p \approx 3100$ kg/m^3 [e.g., *Pysklywec and Cruden*, 2004].

The model lithospheric mantle is composed of a mixture of black Colorific Plasticine®, 3 M® hollow glass microspheres and PDMS [e.g., *Cruden et al.*, 2006; *Riller et al.*, 2012] (Figure 3). Blending plasticine with PDMS increases the density and effective viscosity and adding microspheres decreases the density while also increasing the effective viscosity of the mixture. We also varied the proportions of these components to achieve suitable upscaled values for the lithospheric mantle viscosity and density. A volume percentage mixture of 57% PDMS + 29% black Colorific Plasticene® + 14% 3 M® hollow glass microspheres (class K-1) resulted in a model lithospheric mantle density of $\rho_m \approx 1080$ kg/m^3, which scales up to a natural lithospheric mantle density of $\rho_p \approx 3050$ kg/m^3. The rheological properties of the mixture were measured over the relevant experimental strain rate range (1×10^{-5} to 5×10^{-4}) using an Anton Paar Physica MCR-301 parallel plate rheometer. Results show that the PDMS-based lithospheric mantle analogue material is slightly non-Newtonian, with a power law exponent $n = 1.25$ and an effective viscosity of $\eta_m \approx 2 \times 10^5$ Pa s, equivalent to $\eta_p \approx 1 \times 10^{22}$ Pa s in nature. This gives a viscosity ratio of $\sim$520 with respect to the Natrosol-NaCl solution,
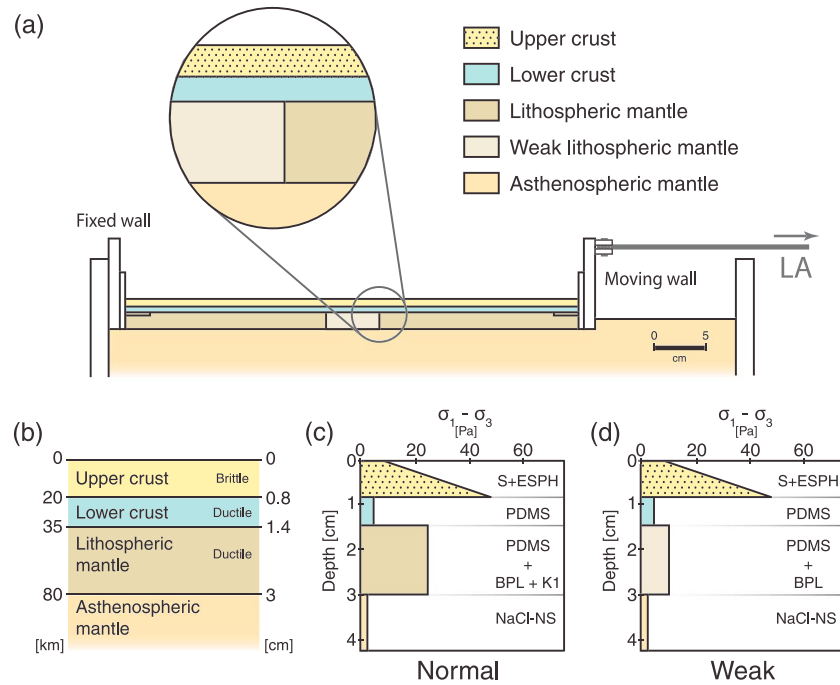
Figure 3. Schematic illustration of the rheological layering of the analogue models and strength profiles of the normal and weak lithospheres. (a) Cross section along the center of the model showing how models are constructed, rheological layering, and approximate location of the weak lithospheric mantle prior to deformation. (b) Natural prototype and scaled down thicknesses for all models (see Table 1 for details). (c and d) Representative strength profiles of the model normal and weak lithospheres. Abbreviations: S = Fine quartz sand, ESPH = Envirospheres® hollow ceramic spheres, PDMS = Polydimethylsiloxane, BPL = Colorific® black plasticine, K1 = 3 M® hollow glass microspheres, NaCl-N = sodium chloride-Natrosol solution.

falling in the upper limit for the range of natural viscosity contrasts between the lithospheric and sublithospheric mantle (~100–500 [*Funiciello et al.*, 2008; *Schellart*, 2008; *Wu et al.*, 2008])

To model a weak lithospheric mantle, we varied the proportions of PDMS and black Colorific Plasticene® to obtain a similar density to the surrounding normal lithospheric mantle but a smaller effective viscosity (Figure 3). The weak lithospheric mantle analogue material comprising a volume percentage mixture of 81.5% PDMS + 18.5% black Colorific Plasticene® has a density of $\rho_m \approx 1075 \text{ kg/m}^3$ and an effective viscosity of $\eta_m \approx 1 \times 10^5 \text{ Pa s}$, equivalent to $\eta_p \approx 5 \times 10^{21} \text{ Pa s}$ (Table 1).

Table 1. Scaling and Experimental Parameters for the Analogue Models[a]

		Thickness		Density		Viscosity		
		Model (mm)	Nature (km)	Model (kg/m³)	Nature (kg/m³)	Model (Pa s)	Nature (Pa s)	Material
Normal Lithosphere								
Upper crust	Brittle	8	20	928	2600	-	-	S + ESPH
Lower crust	Ductile	6	15	982	2760	4×10^4	2×10^{21}	PDMS
Lithospheric mantle	Ductile	16	45	1090	3050	2×10^5	1×10^{22}	PDMS + BPL + K1
Weak Lithosphere								
Upper crust	Brittle	8	20	928	2600	-	-	S + ESPH
Lower crust	Ductile	6	15	982	2760	4×10^4	2×10^{21}	PDMS
Weak lithospheric mantle	Ductile	16	45	1075	3030	1×10^5	5×20^{21}	PDMS + BPL
Asthenosphere		-	-	1100	3100	380	1.9×10^{19}	NaCl-NS
Scaling factors: model/prototype		$L^* = 4 \times 10^{-7}$		$\rho^* = 0.355$		$\mu^* = 2 \times 10^{-17}$		
Time scaling factor		$t^* = \eta^* / (\rho^* \cdot g^* \cdot L^*)$		$t^* = 1.41 \times 10^{10}$		1 h in model ~ 0.8 Ma in nature		
Velocity scaling factor		$v^* = l^*/t^*$		$v^* = 2.84 \times 10^3$		6 mm/h in model ~ 20 mm/yr in nature		
Gravity scaling factor		$g^* = g_m/g_p = 1$						

[a]S = sand; ESPH = hollow ceramic spheres; PDMS = polydimethylsiloxane; BPL = black plasticine; K1 = hollow glass microspheres; NaCl-NS = sodium chloride + Natrosol solution. All layers have dimensions of 440 × 440 mm. Model asthenosphere area is 626 × 626 mm.

The brittle upper crust is modeled using granular materials (Figure 3). To achieve a scaled natural upper crustal density of $\rho_p \approx 2650$ kg/m^3, we mixed quartz sand and hollow ceramic Envirospheres® with bulk densities of 1550 kg/m^3 and 390 kg/m^3, respectively, in the ratio 3.11:1 to obtain a scaled down model upper crustal density of 940 kg/m^3. The graded quartz sand has a homogeneous grain size distribution with 75% of the grains falling between 435 and 500 μm, and the hollow ceramic Envirospheres® have a very homogenous grain size distribution, with 90% of the grains in the 100–150 μm range. Hubbert-type shear box tests for the mixture determined an internal friction angle $\phi < 38°$ and a cohesion value of ~ 9 Pa. The internal friction angle and the negligible cohesion of the mixture make it an appropriate analogue to model brittle upper crust with a Mohr-Coulomb behavior [e.g., *Byerlee*, 1978; *Davy and Cobbold*, 1991; *Schellart*, 2000].

2.3. Experimental Setup and Construction

All experiments start from the same initial state, in which the model lithosphere is attached to two U-shaped walls with internal dimensions of $44 \times 44 \times 3$ cm. One wall is fixed to the side of the acrylic tank wall and the other is pulled by a linear actuator at a controlled divergence rate (Figures 2a and 3). A pivot is fixed on one side of the U-shaped walls and the linear actuator rod pulls the moving wall from the opposite side in an anticlockwise fashion, creating a rotational extensional boundary condition (Figure 2a). The opening of the U-shaped walls creates a free edge in which granular material from the upper crust collapses by gravity (Figure 2b). This unwanted boundary condition of the experimental setup affects a small area that is outside the region of interest (i.e., the surface area selected for deformation monitoring processing) and is therefore not considered to be detrimental to the results. We use an 80:20 wt % paraffin oil in petrolatum jelly mixture [*Duarte et al.*, 2014] as a lubricant between the model lateral boundaries and the confining U-shaped walls to minimize other boundary effects. The lateral side boundary effect caused by the grip between the model lithosphere and the side walls is therefore significantly reduced and is considered negligible for the experiment results.

The model mantle lithosphere and ductile crust layers are constructed to sit within the pair of U-shaped walls, to which they are attached on the sides perpendicular to the extension direction (Figure 3a). The ductile layers are first made separately by allowing them to spread to the desired area and thickness within a rigid frame. Lithospheric mantle linear weak zones are prepared individually using the same technique and are incorporated into the normal lithospheric mantle layer by inserting them into a space created by cutting and removing material. This procedure is done ~48 h before the experiment to allow the normal-weak combined lithospheric mantle material to settle within the rigid frame. Specially designed 4 cm wide horizontal grips are also incorporated along two sides of the lithospheric mantle layer, which is then placed on top of the model asthenospheric mantle, within the U-shaped walls (Figures 2 and 3). The ductile crust layer is then placed on top and the model is left to sit to allow sufficient time to achieve isostatic equilibrium and for air bubbles to dissipate (~7 h). The model upper crust layer is then deposited by sifting granular materials (see section 2.2) from a height of ~15 cm. No manual off scraping is done to prevent alterations in the mechanical properties of the upper crustal layer due to unwanted compaction. Once all model lithosphere layers are in place and in isostatic equilibrium with the asthenosphere, the grips are fastened to the extension-perpendicular sides of the U-shaped walls.

Linear weak zones are incorporated into the model lithospheric mantle with orientations defined by the angle, α, between the trend of the weakness and the orthogonal to the initial extension direction. All linear weak zones had constant width of 5 cm, and α was varied in 15° increments from 0° to 60° (Figure 4). The oblique linear zones were positioned in such way that they cross the center of the model lithospheric plate in map view (defined by the intersection of the two diagonals of the square lithospheric plate; see Figure 4). The final shape and location of the weak zone at the end of each experiment is inferred using control points. Granular material is removed using a vacuum cleaner, and the ductile layers are then gradually removed by cutting them approximately perpendicular to the rift axis. After each section is removed the boundaries of the weak zone are observed in side view, marked on the surface and photographed from above. This is repeated four times, and the final shape of the weak zone is deduced using eight control points.

2.4. Deformation Monitoring and Analysis

Stereoscopic particle image velocimetry (PIV) was used to monitor deformation of the model surface. The PIV system is equipped with three high-speed cameras that provide a spatial resolution of ≥0.1 mm and a
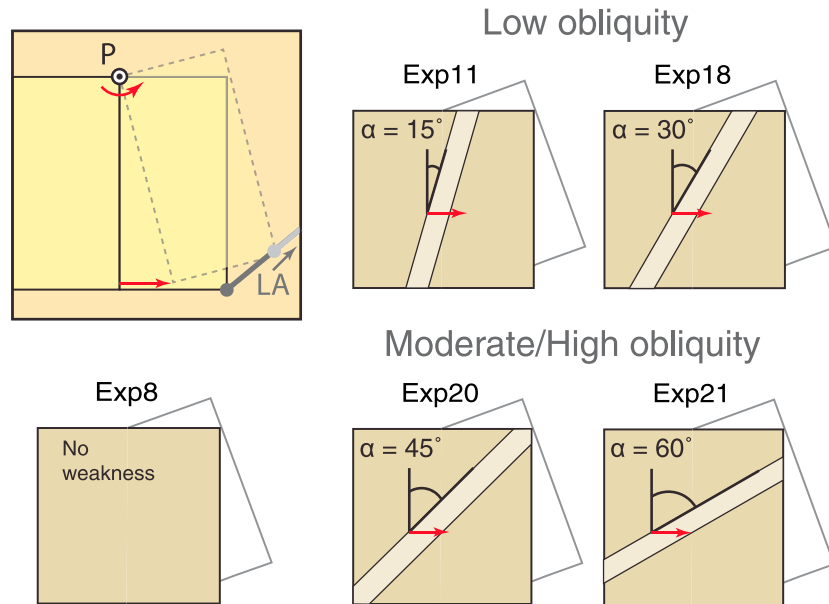
Figure 4. Graphical summary of the boundary conditions for the laboratory experiments presented in this article. (top left) Plan view sketch of the rotational boundary condition, imposed by fixing a pivot (P) at one side of a moveable U-shaped wall and pulling from the opposite side with a linear actuator (LA). (middle and right columns) Lithospheric mantle linear weakness orientation (α) in plan view of the experiments discussed in this work.

temporal resolution of ≥ 0.1 s. Successive PIV images were taken at 2 min intervals during each experimental run. Dark-colored sand grains sifted on top of the model served as passive markers (Figure 2b). Stereo cross correlation [*Adam et al.*, 2005] was used to obtain precise spatiotemporal measurements of incremental and cumulative deformation [e.g., *Boutelier and Cruden*, 2013; *Riller et al.*, 2012; *Schrank et al.*, 2008]. Cumulative data are calculated as the sum of the incremental data. We computed high-resolution displacement fields, and based on the strain tensor,

$$E_{ij} = \frac{\partial V_i}{\partial_j} \text{ with } i \in \{x, y, z\} \text{ and } j \in \{x, y, z\} \tag{2}$$

we calculate the gradient in the vector component i along the j axis. In order to calculate total normal strain on the surface, instead of determining the horizontal normal strain along a single Cartesian coordinate direction [e.g., *Boutelier and Cruden*, 2013; *Chen et al.*, 2016], we consider the 2-D strain matrix

$$\begin{vmatrix} E_{xx} & E_{xy} \\ E_{yx} & E_{yy} \end{vmatrix} \tag{3}$$

and define the normal strain, E_{surf}, on the surface as the largest eigenvalue of the matrix:

$$E_{surf} = \frac{(E_{xx} + E_{yy})}{2} + \sqrt{\left| \frac{(E_{xx} + E_{yy})^2}{4} + \frac{(E_{xy} + E_{yx})^2}{4} \right|} \tag{4}$$

Detailed analysis of the models shows that the initial rupture of the model brittle crust occurs approximately when the incremental $E_{surf} > 1\%$ (e.g., Figure 5a, 5% extension). We therefore define this value as a useful threshold to detect when a structure becomes active or inactive during the experiments, in order to track the migration of the rift tip. Digital elevation models (DEMs) created from the stereoscopic images are compared with top-view digital photographs taken with oblique lightening to improve visualization of fault segments.

3. Results

Fifteen experiments were carried out with initial conditions summarized in Table 2. Five experiments were repeated to test for reproducibility and resulted in similar first-order deformation patterns and evolution
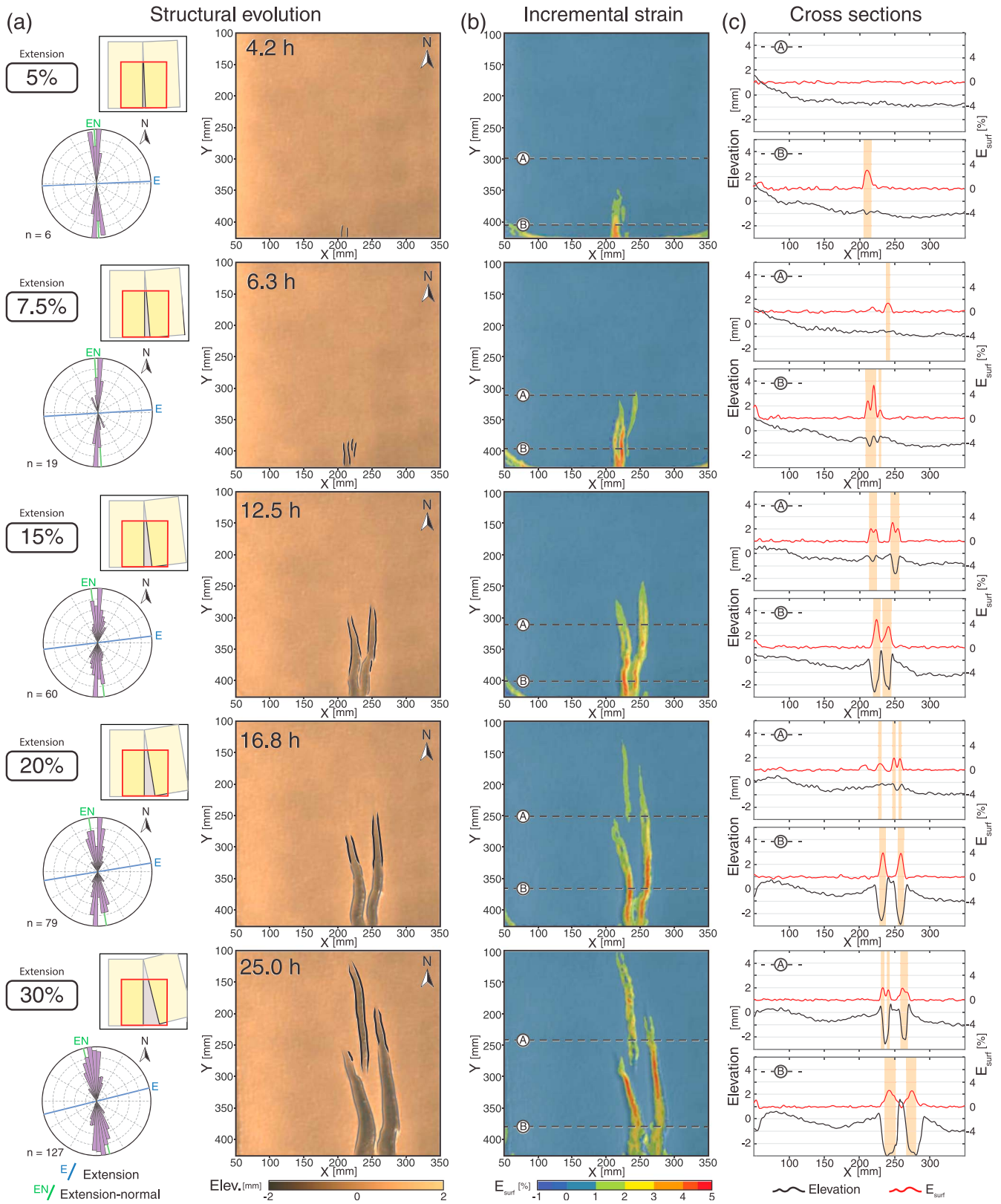
Table 2. List of the Performed Analogue Experiments

Experiment	Weakness Obliquity Angle	Length Scaling Factor	Comment
3	No weakness	6.00E-07	First successful rotational experiment
5	No weakness		Failed due to initial setup
6	No weakness		Failed due to initial setup
8[a]	No weakness	4.00E-07	Similar evolution to Experiment 3
9	0°		Single propagating rift
10	−15°		Rift develops as compartments
11[a]	15°		Development of intrarift block
12	60°		Partitioned deformation
16	15°		15° repetition
17	30°		No development of intrarift block
18[a]	30°		30° repetition; development of intrarift block
19	45°		Partitioned deformation
20[a]	45°		45° repetition
21[a]	60°		60° repetition
22	No weakness		Similar evolution to Experiments 3 and 8

[a]Experiments discussed in this work.

(see Movies S1 to S10 in the supporting information). We focus on the results from five representative experiments (Figure 4), which are subdivided into groups based on the obliquity angle of the linear zone of weakness, α, including one homogeneous reference experiment.

As the apparatus is designed to impose rotational extension, we characterize the different rifting stages according to the maximum imposed percentage of stretching (i.e., displacement of the linear actuator), which occurs at the free side of the model, opposite the fixed pole of rotation (Figures 2a and 3). For practical purposes, we define north as toward the pole of rotation; hence, rift propagation takes place from south to north. The southern margin of the model is hereafter referred as the opening side.

Experimental results are presented in Figures 5 to 9 and are subdivided into three sections: structural evolution (Figures 5a, 6a, 7a, 8a, and 9a), incremental strain (Figures 5b, 6b, 7b, 8b, and 9b) and evolutionary topographic cross sections (Figures 5c, 6c, 7c, 8c, and 9c). Structural evolution is presented in top view as line drawings of structures on color digital elevation models, together with the corresponding fault distribution for each stage illustrated as rose diagrams of fault azimuths. Incremental strain is also presented as top views as maps of incremental normal strain (E_{surf}) on the model surface draped over a shaded relief DEM for each stage. The linear weakness boundaries, when present, are marked as dashed lines in all top-view figures. We plot two profiles of the surface elevation and normal strain on the model surface (E_{surf}) for each stage, along sections indicated as dashed lines A and B in Figures 5b, 6b, 7b, 8b, and 9b. Incremental strain values that exceed the previously defined threshold ($E_{surf} > 1\%$) are indicated by orange shading to highlight areas where deformation is active at each stage.

3.1. Reference Experiment-Homogeneous Lithosphere (Experiment 8)
3.1.1. Early Stages
After 5% extension, short, normal faults formed perpendicular to the extension direction as strain localized at the south central end of model (Figures 5a and 5b: 5% extension). During this stage, extension was accommodated on these major boundary faults as they propagated northward. At 7.5% extension, incremental strain measurements show the initiation of a second, subparallel rift segment that propagated toward the pole of rotation (Figure 5b: 7.5% extension). Increasing stretching activated linear normal linear faults that

Figure 5. Evolution of deformation for reference experiment eight with homogeneous lithosphere (i.e., no lithospheric mantle weakness). (a) Structural interpretation presented in top-view DEMs. Black lines are active normal faults, and grey lines are inactive normal faults at each stage. Rose diagrams at bottom left show normalized fault distribution with 36 bins (i.e., each bar represents a 5° azimuth range) weighted for the fault length. Colored lines are the extension direction (E), extension-normal direction (EN), and the initial orientation of the linear weakness (W), when present. Schematic drawing in the top left illustrates the amount of rotation of the model in plan view. Red squares in small insets indicate the area analyzed. (b) Maps of incremental normal strain on surface (E_{surf}) for each stage. Location of profiles A and B shown in Figure 5c are indicated by black dotted lines. (c) Surface elevation (black) and incremental normal strain on surface (red) profiles. Shaded areas indicate sections that are actively accommodating extension at each stage (i.e., $E_{surf} > 1\%$, see text for details). For detailed model evolution, see Movie S1 in supporting information.
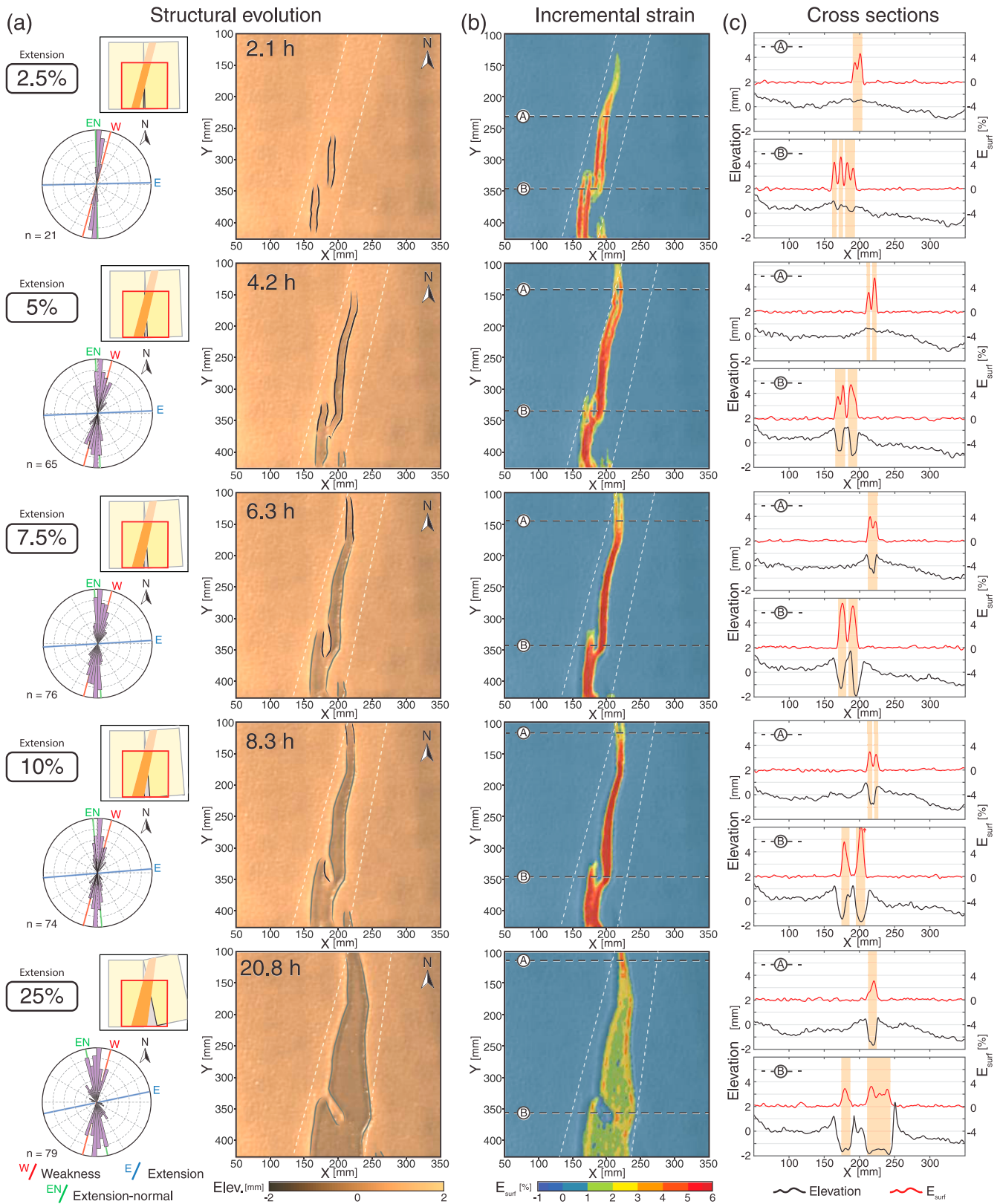
Figure 6. Evolution of deformation with a low obliquity ($\alpha = 15°$) linear weakness zone (Experiment 11), illustrated as in Figure 5. (a) Schematic drawing in the top left illustrates the amount of rotation of the model and approximate location of the lithospheric mantle linear weakness. Red squares in small insets indicate area analyzed. Boundaries of the linear weakness are shown as white dotted lines in Figures 6a and 6b. For detailed model evolution, see Movie S2 in supporting information.
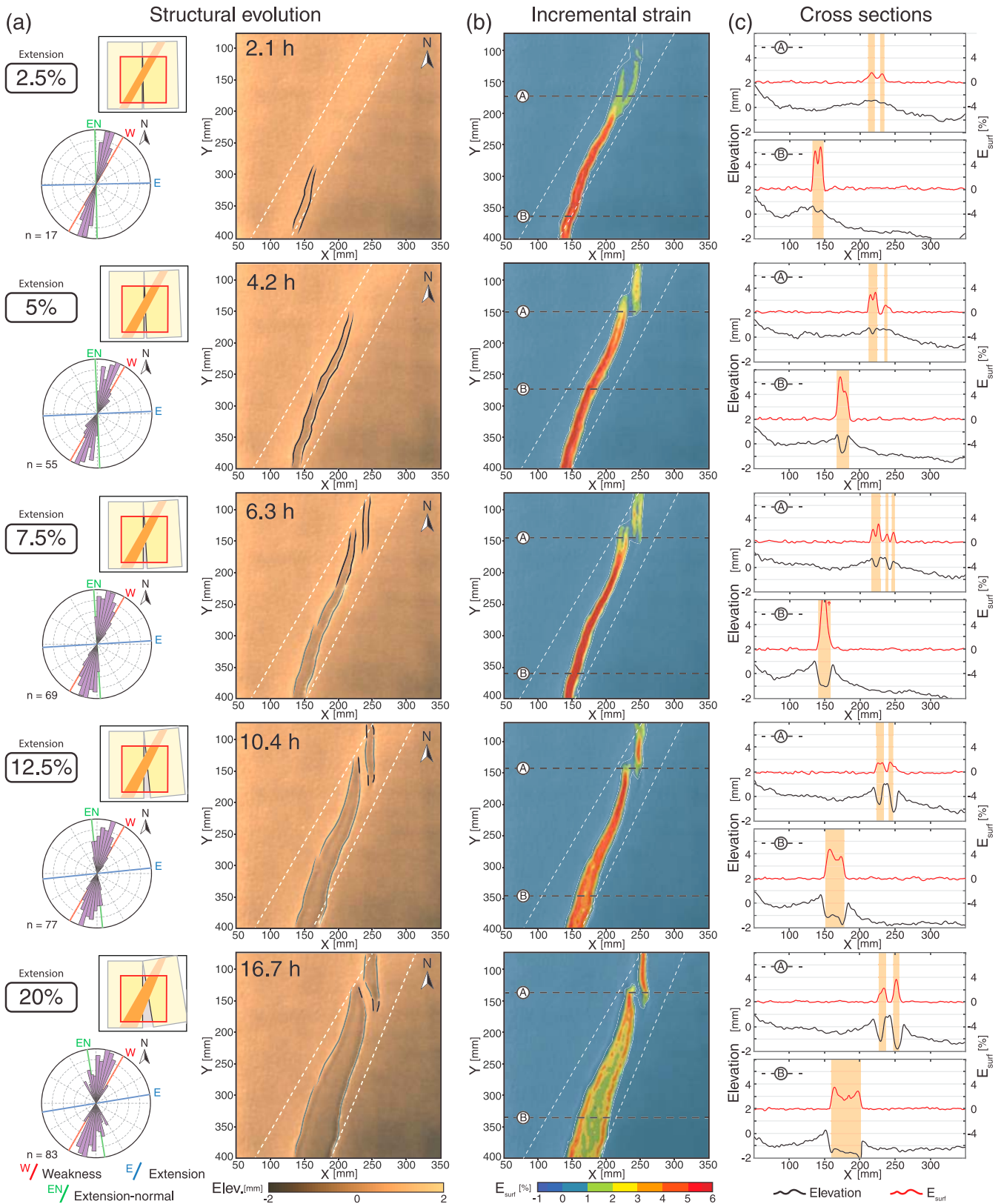
Figure 7. Evolution of deformation with a low obliquity ($\alpha = 30°$) linear weakness zone (Experiment 18), illustrated as in Figures 5 and 6. (a) Schematic drawing in the top left illustrates the amount of rotation of the model and approximate location of the lithospheric mantle linear weakness. Red squares in small insets indicate area analyzed. Boundaries of the linear weakness are shown as white dotted lines in Figures 7a and 7b. For detailed model evolution, see Movie S3 in supporting information.
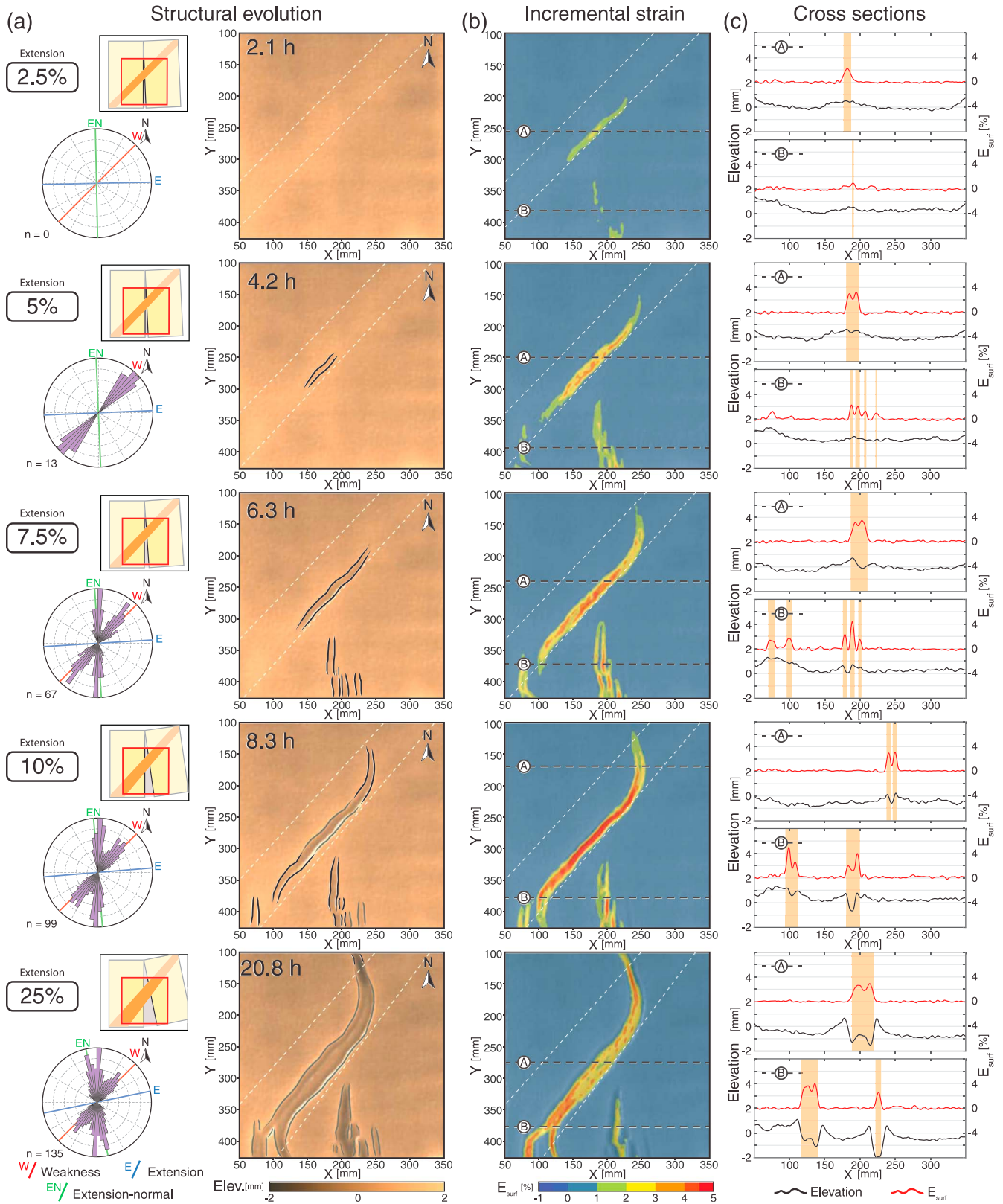
Figure 8. Evolution of deformation with a moderate obliquity ($\alpha = 45°$) linear weakness zone (Experiment 20), illustrated as in Figures 5 and 6. (a) Schematic drawing in the top left illustrates the amount of rotation of the model and approximate location of the lithospheric mantle linear weakness. Red squares in small insets indicate area analyzed. Boundaries of the linear weakness are shown as white dotted lines in Figures 8a and 8b. For detailed model evolution, see Movie S4 in supporting information.
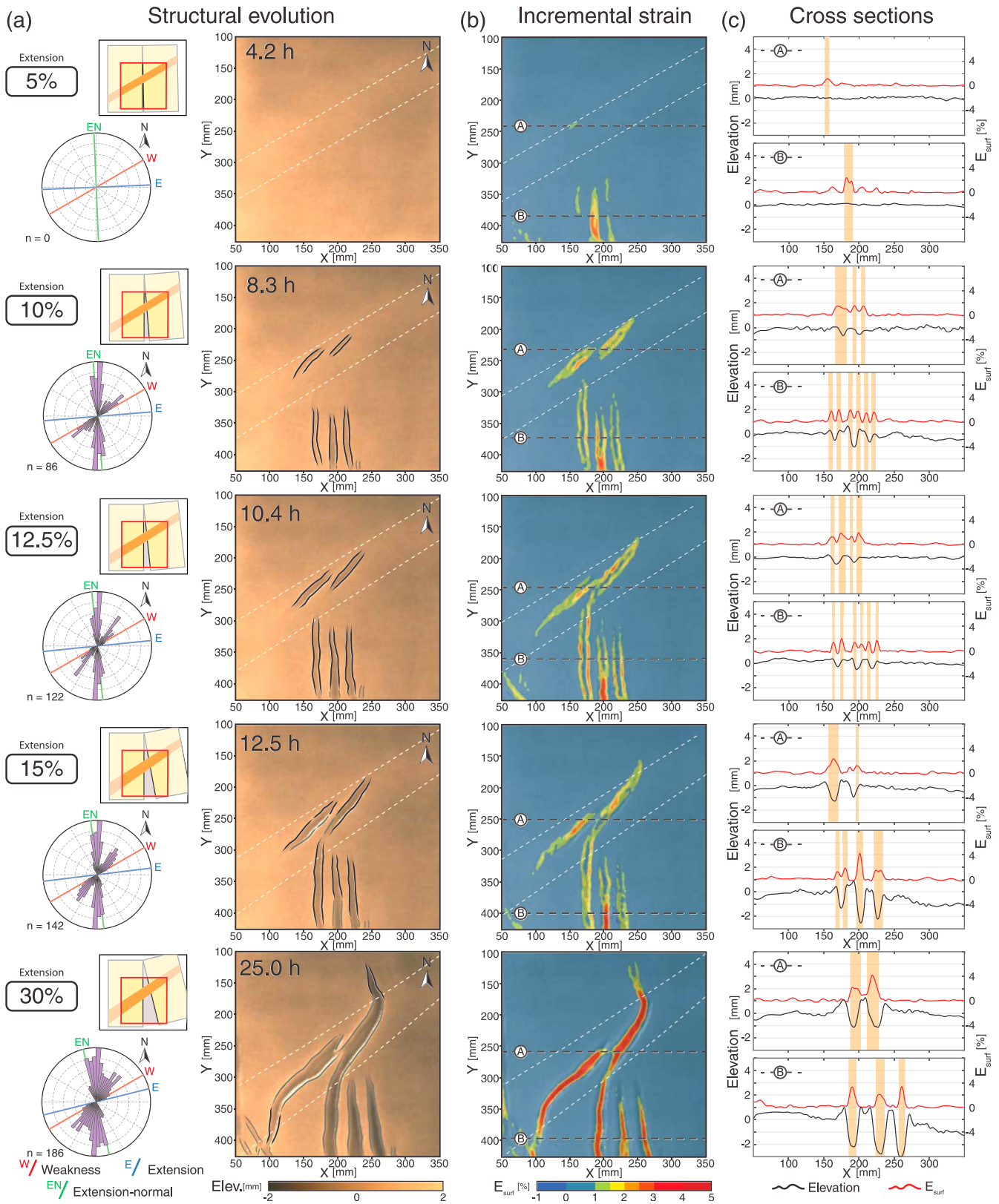
Figure 9. Evolution of deformation with a high obliquity ($\alpha = 60°$) linear weakness zone (Exp. 21), illustrated as in Figures 5 and 6. (a) Schematic drawing in the top left illustrates the amount of rotation of the model and approximate location of the lithospheric mantle linear weakness. Red squares in small insets indicate area analyzed. Boundaries of the linear weakness are shown as white dotted lines in Figures 9a and 9b. For detailed model evolution, see Movie S5 in supporting information.

bound both segments and led to the development of two V-shaped graben with northward propagating tips. Although the eastern graben developed later, its propagation was faster than the western graben (cf. Figures 5a and 5b: 7.5–15% extension). Cross sections of surface elevation and incremental strain in the southern half of the model at 15% extension (Figure 5c) indicate that the two rift depressions have similar geometry in the southern end, with the western graben recording higher incremental strain. However, toward the center of the model the eastern graben accommodates more extension and is bound by faults with greater throws compared to the western graben. Orientation analysis indicates that the boundary faults of the V-shaped basins strike approximately perpendicular to the stretching direction as they propagate (Figure 5a).

3.1.2. Advanced Stages

The main boundary faults opposite the pole of rotation were active until ~15% extension, when strain gradually localized in the floors of the southern parts of the two early-formed rift depressions as they became wider (Figures 5a and 5b: 15–20% extension). With increasing extension, the bounding faults of the two graben structures propagated northward and the separation between the rift segments increased. Northward propagation of the western graben terminated when it reached the center of the model after ~20% extension (Figures 5a and 5b). Subsequent extensional deformation in the model was transferred to the eastern graben and to a newly formed central graben located between the eastern and western graben (Figures 5a and 5b: 20–30% extension). As extension continued, the rift-subparallel bounding faults of the central graben propagated to the north and south. Ongoing deformation was entirely accommodated by the central graben as it propagated toward the pole of rotation. At very advanced stages (>30% extension) the main rift boundary faults in the southern half of the model became inactive as strain became localized in the rift depressions (Figures 5b and 5c: 30% extension). These areas of lithospheric thinning also became wider to the south. This trend continued until maximum extension of the experiment was reached (~45%), at which point no further evidence of fault nucleation between rift zone compartments was observed.

3.2. Low Obliquity Weakness Zone (Experiments 11 and 18)

3.2.1. Experiment 11

3.2.1.1. Early Stages

Experiments with a low obliquity ($\alpha = 15°$) linear weakness zone are characterized by early development (2.5% extension) of two north-south oriented rift segments, delineated by linear normal faults that strike at intermediate angles between the trend of the linear weakness zone and the direction perpendicular to the initial extension direction (Figure 6a: 2.5% extension). Elongated domains of incremental strain illustrate how these normal faults formed approximately in the center of the linear weakness zone and delimited a southwest and a central graben (Figures 6a and 6b: 2.5% extension). Extension was progressively accommodated by these structures as their throw increased and as they propagated both north and south. After 5% extension the northern tip of the southwest graben reached its maximum propagation point (Figure 6a). Comparison between incremental strain measurements at 2.5% and 5% extension shows that the two en echelon-oriented rift segments within the weak zone propagate sideways and start to overlap (Figure 6a: 5% extension). The deflection in the strike of the faults as they overlap is probably due to rift interaction, which is a consequence of the close proximity of the two rift segments [cf. *Zwaan et al.*, 2016]. With further extension, the main boundary faults in the center of the model propagated northward with an orientation that gradually became aligned with the trend of the weakness zone (Figures 6a and 6b). By 7.5% extension, surface elevation and strain profiles (Figure 6c: 7.5% extension) indicate that the only active fault segments at 7.5% extension were those formed due to this northward migration of the central V-shaped basin. At this stage strain progressively localized in the narrow rift depressions to the south of the model.

3.2.1.2. Advanced Stages

The activity of the boundary faults diminished with progressive deformation, showing no substantial variations in vertical throw after 7.5% extension (Figure 6c). At this stage, strain became highly localized in the center of the rift depression and extension was consequently accommodated by lower crustal and lithospheric mantle stretching within the linear weakness zone. This resulted in a different amount of thinning between the normal and weak lithosphere. The boundary faults were oriented perpendicular to the direction of extension as they grew toward the model pivot point (proxy for pole of rotation). Observations on the overall evolution of deformation show that strain is focused in the linear weakness zone for the majority of the experiment. No substantial change in deformation style was observed with progressive stretching after

10% extension. However, a rotating intrarift block developed with increasing extension (Figure 6a: 10–25% extension). The rift segments that nucleated at early stages (<5% extension) delimit a horst that rotated counterclockwise about an independent pole of rotation located on the west margin of the rift. The final stages of the experiment show a wide distribution of strain in the thinned lithosphere of the rift floors, and their margins are characterized by progressive upward flexure due to local isostasy associated with the rift flanks (Figures 6b and 6c). Extensional structures only developed outside the weak zone at late stages and resulted in the anastomosing geometry of the main rift boundary faults (see Movie S2 in supporting information).

3.2.2. Experiment 18

Experiment 18 ($\alpha = 30°$) developed a very similar deformation evolution to Experiment 11 in terms of compartmentalization and strain partitioning, with slight differences in the timing (i.e., percent of extension) at which each step in the evolution took place. Comparison between Experiment 11 ($\alpha = 15°$) and Experiment 18 ($\alpha = 30°$) shows that the southernmost end of the weak zone is closer to the point of maximum extension in experiments with a lower obliquity linear weakness (Figure 4). This results in an earlier widening of the weak zone and causes deformation to stay localized within it (cf. Figures 6 and 7). In Experiment 18, an elongated rift segment that formed subparallel to the linear weak zone accommodated most of the extension at early stages (Figures 7a and 7b: 2.5–5% extension). Strain localized along the linear weakness zone and progressive deformation led to the development of a second, north-south oriented graben. This resulted in the formation of an intrarift block in the northern part of the model (Figures 7a and 7c: 7.5% extension). The main difference between Experiments 11 and 18 was in the location of the counterclockwise rotating intrarift block, which formed closer to the pole of rotation in Experiment 18. The geometry of a 30° oriented weakness zone results in a greater distance along the center of the model between the opening side of the model and the linear weak zone boundary. The southernmost section of the weak zone in Experiment 18 is farther away from the point of maximum extension than in Experiment 11 (Figure 4). As a result, strain partitioning and compartmentalization occurred at later stages and closer to the pole of rotation (Figure 7a: 12.5–20% extension), indicating that the position of the weak zone influences the resulting structural pattern in addition to the angle of obliquity. The higher rotation rate of the intrarift block in Experiment 18 is due to its proximity to the model pivot point.

3.3. Moderate Obliquity Weakness Zone (Experiment 20)

3.3.1. Early Stages

Incremental strain measurements at early stages of the $\alpha = 45°$ experiment (Figure 8b: 2.5% extension) show two domains of incipient rift formation and propagation. Deformation was localized along the south eastern margin of the linear weak zone during this stage, as illustrated by the 45° striking oriented domain of incremental strain in the center of the model (Figures 8a and 8b). Minor domains oriented perpendicular to the extension direction accommodated deformation in the southern part of the model. As extension increased, the central rift zone propagated toward both the southwest and northeast, parallel to the linear weak zone, along which normal faults initiated after 5% extension, accommodating most of the deformation (Figures 8a and 8b). At this stage, the extension-perpendicular domains of incremental strain increased steadily, but no rupture of the brittle upper crust was observed in the southern end of the model until 7.5% extension, when ongoing deformation in the area resulted in the development of a series of short, displacement-perpendicular rift segments (Figure 8a). The activity of the boundary faults associated with these rift segments is greatest between ~7.5% and ~12.5% extension. The normal faults of the central graben also propagated in both directions during this stage and the tips of the central rift began to rotate progressively into alignment with the extension-perpendicular direction (Figures 8a and 8b: 7.5–10% extension), producing a sigmoidal rift segment that remained within the weak zone until advanced stages of the experiment.

3.3.2. Advanced Stages

After 10% extension, strain continued to be largely accommodated by the central rift segment, with increased vertical throw on its boundary faults and subsequent deepening of the rift floor (Figures 8a and 8b). However, the activity of the delineated normal faults decreased after ~15% extension. This resulted in the progressive localization of strain toward the rift depression, resulting in differential thinning of the lithosphere. The earlier formed north-south graben structures in the south were aborted as extension continued, suggesting that deformation was entirely transferred to the boundary of the linear weak zone (Figure 8b: 25% extension). No new rift segments were created between 25% and the maximum extension (~45%). Upward flexure of the thinned lithosphere was observed at late stages, as in the low obliquity experiments.

3.4. High Obliquity Linear Weakness (Experiment 21)

The experiment with a highly oblique linear weakness zone ($\alpha = 60°$) showed similar behavior to the moderate obliquity experiment ($\alpha = 45°$). Two domains of rift formation were also observed in the model, with some variations in the timing of the development of rift-related faults. The most relevant differences are described below.

3.4.1. Early Stages

Deformation was initially localized parallel to the northern boundary of the weak zone (Figures 9b and 9c: 5% extension) and in several subparallel rift segments that developed perpendicular to the extension direction in the southern part of the model, which then propagated with increasing stretching toward the pole of rotation (Figures 9a and 9b: 5–10% extension). At 10% extension, the weak zone in the center of the model is associated with the development of two deformation compartments with orientations that are intermediate between the trend of the discontinuity and the extension-perpendicular direction (Figure 9a: 10–12.5% extension). Comparison with Experiment 20 ($\alpha = 45°$) shows that these rift segments formed in the center of the model but are shorter in length in Experiment 21. However, the overall sigmoidal shape of the rift is maintained at advanced stages (cf. Figures 8 and 9). These central structures propagated both southwest and northeast after 10% extension and, together with the displacement-perpendicular segments in the south, actively accommodate deformation until ~15% extension (Figures 9a and 9b).

3.4.2. Advanced Stages

After 15% extension, the propagation rate of the V-shaped basins in the southern part of the model diminished and deformation was progressively transferred to the central oblique graben structures (Figures 9a and 9b). The length of the normal faults that delimit these graben increased steadily and their orientation gradually changed. As in the moderate obliquity experiments, these boundary faults eventually became aligned with the displacement-perpendicular direction (Figures 9a and 9b: 15–30% extension). With ongoing deformation, the easternmost central graben merged with the main V-shaped basin as they propagated in opposite directions (Figure 9a: 30% extension). The number of rift segments stabilized during the advanced stages (+30% extension) when basin widening and strain localization in rift interiors was observed.

4. Synthesis and Discussion

The experimental results described above demonstrate that the structural evolution and partitioning of strain in extending continental lithosphere is strongly influenced by the presence of linear rheological discontinuities. Since the external boundary conditions in each experiment were the same, we can compare the different model results to gain insights on how the orientation of linear lithospheric weaknesses influences rift propagation. Figure 10 compares cumulative strain over time in the experiments as a function of linear weak zone orientation. It is observed that the presence of a linear zone of weakness in the lithosphere has a profound effect on the resultant architecture and strongly controls strain partitioning in propagating rifts. The strength of the normal lithospheric mantle in our models is approximately 2 times greater than that of the weak lithospheric mantle (Figure 3 and Table 1), suggesting that even a relatively small difference (i.e., values within the same order of magnitude) in the strength of the layers will induce strong strain partitioning as observed in the experiments. When present, the boundary of the weak zone always localized deformation at some stage during the experiments. Previous analogue experiments with different experimental setups have also studied the effect of mechanical discontinuities during oblique rifting [*Tron and Brun*, 1991] and in rift basins with a rotational component [*Philippon et al.*, 2014]. Consistent with our results, these studies have similarly concluded that the resulting structural pattern can only be explained by considering the presence of inherited structures or rheological heterogeneities in addition to the geodynamic setting.

In terms of deformation evolution, we define three end-members: homogeneous lithosphere, low obliquity, and moderate/high obliquity linear weaknesses. The key differences and observations between the experiments, broken down by these three categories, are summarized in Figure 11.

The change in the extension direction over time strongly controls the evolution of deformation and needs to be investigated jointly with the presence of a weak zone to understand how rifts propagate. Previous analogue modeling with a comparable linear weak lithospheric mantle [e.g., *Agostini et al.*, 2009; *Autin et al.*, 2010; *Corti*, 2008] but with a translational rather than a rotational boundary condition provided detailed analysis of fault patterns but did not characterize how faults propagate along the rift axis over time at large scales.
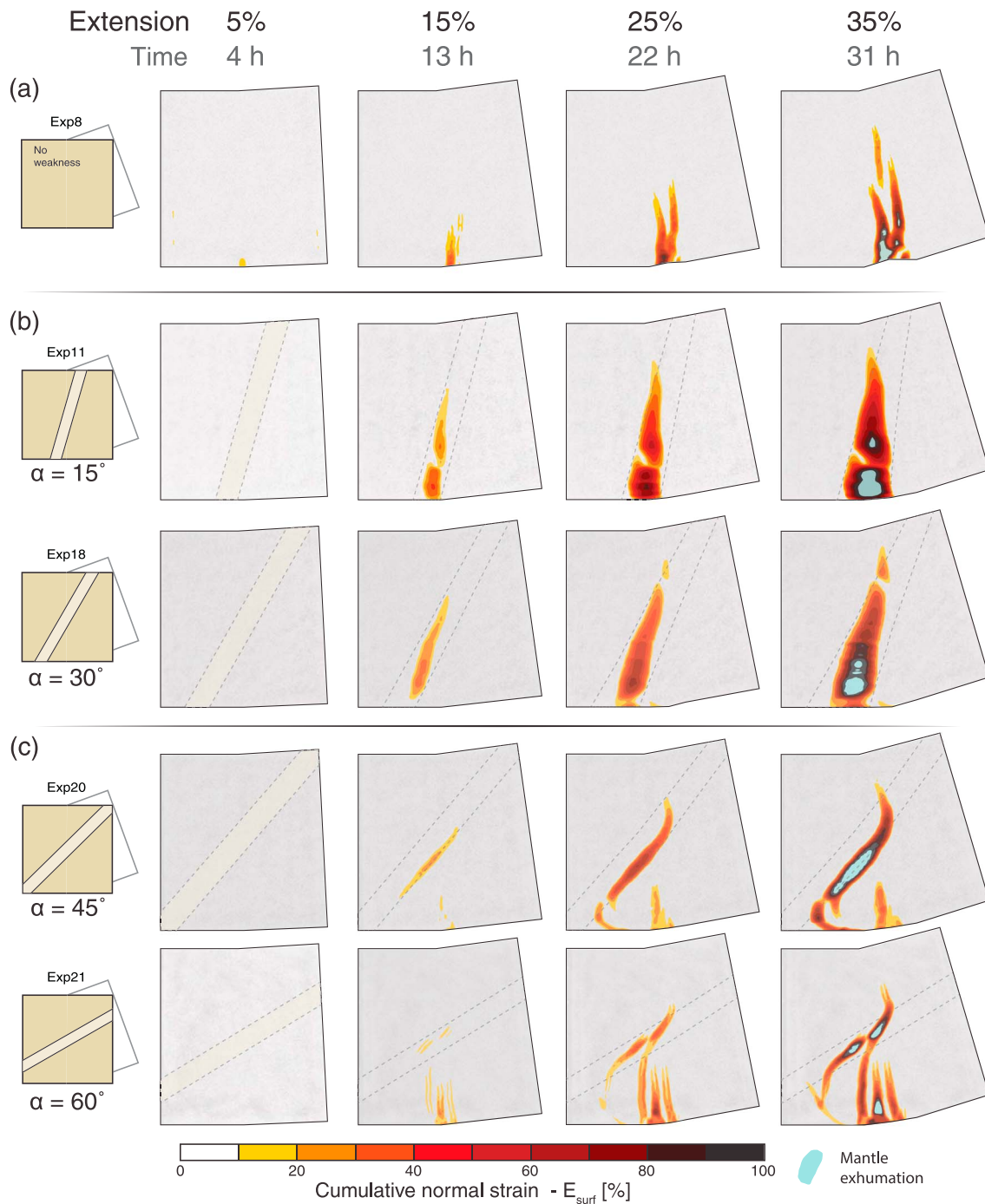
Figure 10. Cumulative strain maps for each experiment after 5%, 15%, 25%, and 35% extension. Strain values are normalized such that the maximum reached strain in each experiment is 100%. Three end-members are defined based on the overall deformation evolution of the models: (a) homogeneous lithosphere, (b) low obliquity, and (c) moderate/high obliquity. Color scale indicates cumulative normal strain on surface (E_{surf}). For cumulative strain evolution, see Movies S1–S5 in supporting information.

In the reference experiment (Experiment 8, no weakness), extension was progressively accommodated in narrow segments as deformation propagated toward the pole of rotation while ongoing rotation resulted in highly extended areas at the opening side of the model, where early rupture and mantle exhumation occurred. However, when a lithospheric mantle weakness was present, the overall evolution of deformation became more complex and crustal stretching did not necessarily increase with progressive propagation of a
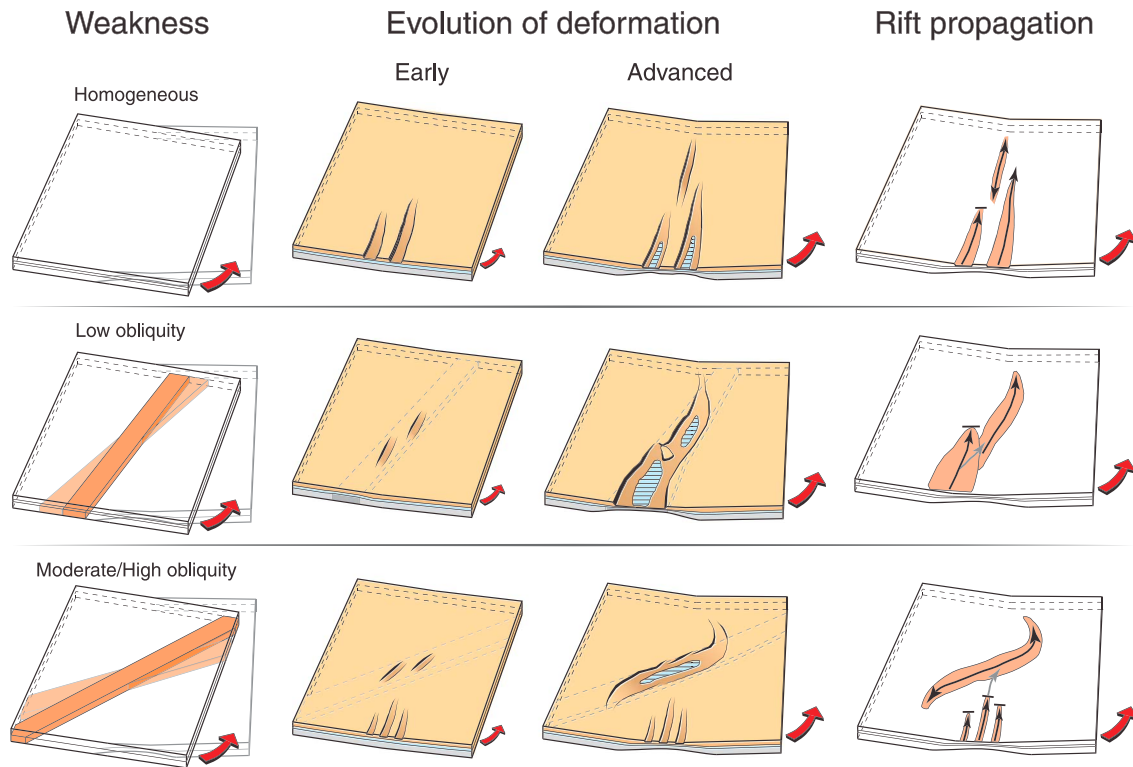
Figure 11. Summary of experimental findings in terms of evolution of deformation and rift propagation as a function of linear weakness obliquity.

rift. This is in agreement with *Martin* [1984] who proposed that continents should react differently in the rifting process when rifts cross older geotectonic features.

A homogeneous model lithosphere (i.e., no lithospheric mantle weakness) accommodated extension by forming V-shaped extensional basins with tips that propagated at constant rates toward the pole of rotation. Boundary faults delimiting these V-shaped basins that formed at early stages were progressively aborted and strain subsequently localized closer to the moving U-shaped wall and toward the pole of rotation. Normal faults that formed in the center of the model propagated both toward and away from the pole of rotation. Although the asymmetric setup of the apparatus may tend to favor eastward migration of active structures, the final structural pattern of the homogeneous model lithosphere experiment is essentially symmetric. Therefore, we consider this model limitation to have a second-order influence on the experimental outcomes and that our setup is an effective means to simulate rift propagation toward a pole of rotation. Furthermore, having a fixed plate and a moving plate is analogous to the natural cases discussed below (see section 4.1).

Models with low obliquity lithospheric weaknesses localized deformation more effectively along the rift axis (i.e., perpendicular to the extension direction) in comparison to the homogeneous and moderate/high obliquity models. Extension was accommodated in short, narrow domains at early stages by bounding faults with trends that are in between those of the linear weakness zone and the extension direction. This is consistent with observations based on strain and stress field analysis in natural examples of slow spreading ridges [e.g., *Fournier et al.*, 2004; *Fournier and Petit*, 2007]. The bounding faults nucleated and propagated at regular rates until strain was transferred to rift depressions. This consequently produced areas of hyperextended lithosphere, and, as a result, these experiments developed considerably wider rifts and showed larger isostatic adjustments during deformation. The rotational boundary condition prevented the nucleation of early rift compartments over time and promoted the formation of an independently rotating intrarift segment. The location of this segment will depend not only on the orientation of the linear weakness zone and the geometry of the model but also on the position of the oblique weak zone within the system. In the experiments presented here the linear weak zone always crosses the central point of the model lithosphere. Thus, when the linear weak zone is highly oblique, the southernmost point of the weak layer is farther away from the point of maximum extension (i.e., at the opening side and opposite the fixed pole of rotation). In

comparison to low obliquity cases, this will favor considerably more strain partitioning between structures in the southern end of the model compared to those proximal to the weak zone.

Partitioning of deformation in moderate/high obliquity weakness experiments was more complex. Extension was initially accommodated by two different features. As in the homogeneous reference lithosphere model, subparallel V-shaped basins propagated toward the pole of rotation, while extension in the model center was accommodated by weakness zone subparallel graben structures. Progressive stretching led to the abandonment of the early V-shaped basins and transfer of strain to structures developed in the vicinity of the weak lithosphere zone boundary. However, structures in high obliquity models would be different if the weak zone was placed closer to the opening side of the model. The relative position of the weak layer with respect to the point of maximum extension also plays an important role in the resulting structural patterns but is beyond the scope of this study.

4.1. Comparison With Natural Examples

We compare our experimental results with selected natural examples in which divergence rates or rheological boundary conditions are in good agreement with the general evolution of deformation in our models, despite some differences in their tectonic settings.

4.1.1. Vavilov Basin, Tyrrhenian Sea

The Vavilov Basin is located in the southern domain of the Central Mediterranean Tyrrhenian Sea, where south-eastward rollback of the Ionian plate beneath the Calabrian Arc (Figure 12a) formed a Neogene-Quaternary back-arc basin [*Malinverno and Ryan*, 1986; *Faccenna et al.*, 1996]. The fault pattern in the Vavilov Basin is characterized by a series of linear normal faults with strikes that change gradually from NE-SW in the west to NW-SE in the east (Figure 12a), defining a radial distribution about a pole of rotation to the north in the vicinity of Rome [*Milia et al.*, 2016]. This fault pattern is comparable to the results of Experiment 8 (Figures 5 and 12b). The triangular shape of the Vavilov Basin resulted from different rates of extension since the middle Miocene, which increased from ~20 mm/yr in the northern Tyrrhenian Sea to ~60 mm/yr in the southern Tyrrhenian Sea [*Malinverno and Ryan*, 1986; *Patacca et al.*, 1990], causing the migration and rotation of the finite extensional axis [*Mattei et al.*, 1996]. The strong asymmetry of the basin is related to the curvature of the retreating trench and to an along strike variation in subduction regime, being deeper and steeper to the south [*Faccenna et al.*, 1997; *Finetti*, 1982]

Although the general evolution of the Vavilov basin is well constrained, the fault pattern within the basin is difficult to interpret due to its complex kinematic history. Therefore, the timing and mechanical relationship between the major faults is matter of debate. Analysis of geophysical and geological data from the Vavilov Basin [*Milia et al.*, 2016] indicates an eastward migration of deformation, where the oldest normal faults in the west of the basin were active until displacement was relayed to the central basin and finally to faults that bound the eastern margin of the basin. This interpretation is consistent with the deformation evolution observed in Experiment 8 (Figures 5 and 12a), in which after 20% extension the delimiting boundary faults of the western graben became inactive and deformation was transferred to the eastern graben and to a newly developed central basin (Figures 5 and 12a). This initial west to east gradient is analogous to the history of the Vavilov Basin [*Milia et al.*, 2016], but at later stages in Experiment 8 fault activity switches to a central graben (Figure 5a), which differs from the natural example. However, when this experiment was repeated, a west to east gradient was also observed and two new graben formed at late stages to the east of the main rift (Experiment 22; see Movie S6 in the supporting information).

Highly stretched fragments of continental crust that characterize the southern domain of the Tyrrhenian Sea [*Rosenbaum and Lister*, 2004] show a close match with the advanced stages (>30% extension) of Experiment 8, in which ongoing deformation led to a complete rupture of the upper crust in the southern half of the model. As shown in the cumulative strain diagram for Experiment 8 (Figure 10a), two triangular-shaped sections in this area of the model correspond to sections of hyperextended crust that gave rise to mantle exhumation, favored by localization of strain in the lithosphere-thinned rift depressions after ~30% extension (Figure 5b). This is consistent with the observation of exhumed serpentinized upper mantle peridotites [*Bonatti et al.*, 1990; *Kastens et al.*, 1987; *Milia et al.*, 2013] and mid-ocean ridge basalts [*Kastens et al.*, 1988; *Robin et al.*, 1987] in the southern Vavilov basin, which are attributed to relatively large bulk extension in this area. Overall, the eastward migration of hyperextended crust sections documented in the experiments (Figure 10a) is also similar to the evolution of the Vavilov Basin, in which mantle exhumation started in the
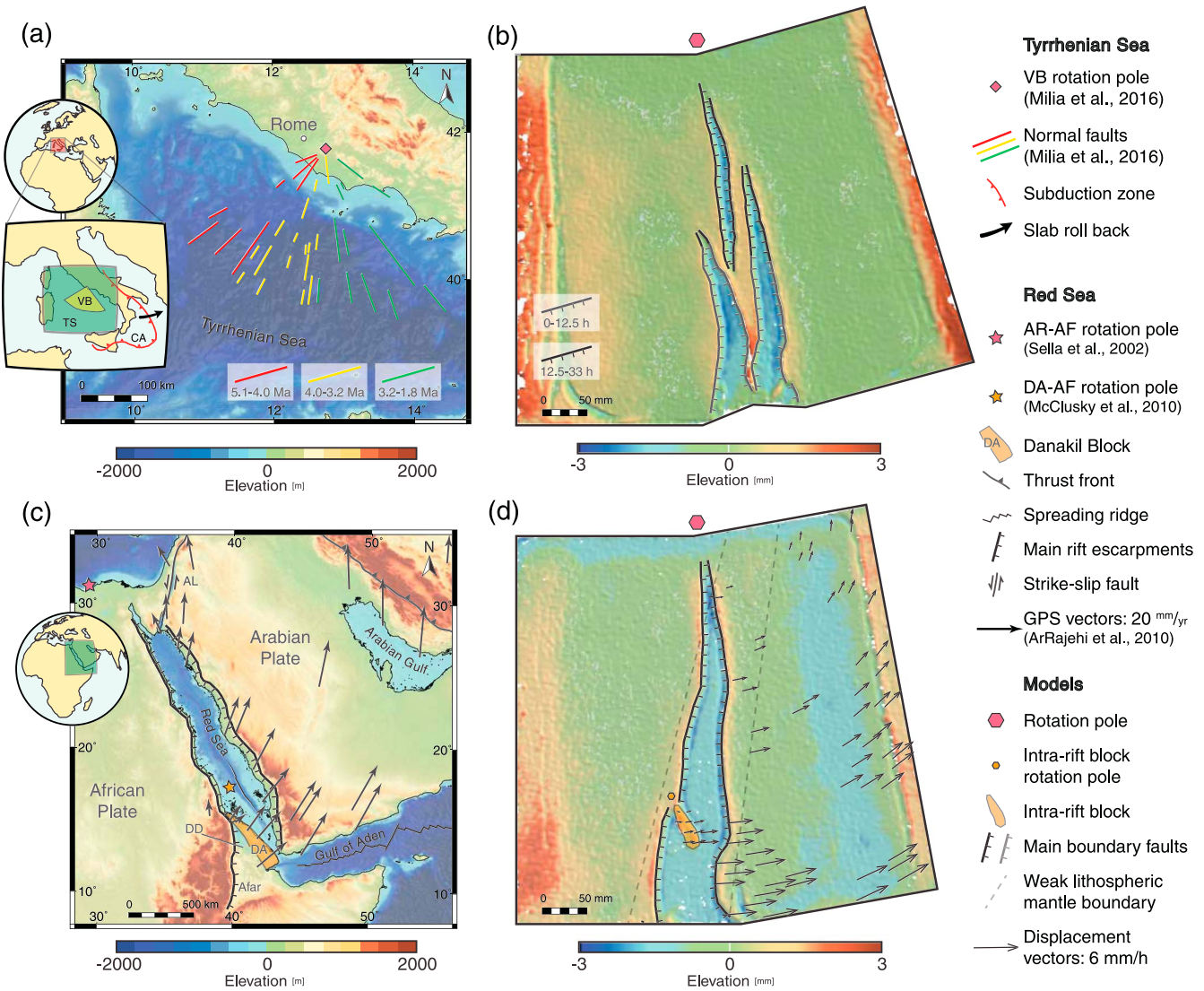
Figure 12. Comparison between model results of Experiments 8 and 11 and selected natural examples of rifting with a rotational component. (a) Bathymetric and topographic map of the Vavilov Basin, Tyrrhenian Sea. Rollback associated to the subduction beneath the curved Calabrian Arc (CA) caused a strong anticlockwise motion that gave rise to the fan-shaped Vavilov Basin. Normal faults, colored as a function of age as interpreted by *Milia et al.* [2016], indicate an eastward time migration of extension. (b) Elevation map of Experiment 8 at 40% extension. Delimiting boundary faults are colored as a function of experimental time in which they were actively accommodating extension. The early developed western graben propagated northward until they became inactive after 20%. Deformation was progressively transferred to the eastern and central grabens. (c) Bathymetric and topographic map of the Red Sea-Gulf of Aden rift system. GPS vectors [*ArRajehi et al.*, 2010] indicate an anticlockwise rotation of Arabia with respect to Africa. Rotation pole is located in the northern coast of Egypt [*Sella* et al., 2002]. The Danakil Block (DA) has an anticlockwise rotation motion about an independent rotation pole, located in the southern Red Sea [*McClusky et al.*, 2010]. (d) Elevation map of experiment 11 at 20% extension. Displacement vectors of the model shows close similarity with GPS vectors of Arabia with respect to Africa (Figure 12c). Deflections in the main boundary faults related to the weak lithospheric mantle also resemble the observed morphology of the main rift escarpments in the southern Red Sea (Figure 12c). VB = Vavilov Basin; TS = Tyrrhenian Sea; CA = Calabrian Arc; AL = Aqaba-Levant transform boundary; DD = Danakil Depression.

Lower Pliocene and subsequently migrated eastward [*Milia and Torrente*, 2015]. A similar stepwise eastward migration of extension has been interpreted for the Latium offshore basin, in the Northern Tyrrhenian Sea [*Buttinelli et al.*, 2014].

4.1.2. Red Sea-Gulf of Aden Rift System

Based on seafloor magnetic anomaly patterns, *McQuarrie et al.* [2003] established that convergence between the Arabian and Eurasian plates has been effectively constant at 20–30 mm/yr over the last 56 Ma. The convergence rate between the African and Eurasian plates decreased to <10 mm/yr in the period 25–30 Ma, coeval with the initiation of the Afar Triple Junction and opening of the Red Sea [*ArRajehi et al.*, 2010]. These

studies also indicate that the relative motion of Africa and Arabia increased by 70% (i.e., ~17 mm/yr) at ~13 Ma and has remained approximately constant since then (Figure 1).

Active rifting in the Gulf of Suez was abandoned in the Middle Miocene (~14 Ma) after Arabia collided with Eurasia, when plate motion was transferred to the Aqaba-Levant transform boundary (Figure 1b). At this time, the Red Sea switched from rift-normal movement (N60°E) to highly oblique extension, parallel to the N15°E oriented Aqaba-Levant transform fault [*Bosworth et al.*, 2005]. The closure of the Neotethys Ocean played a substantial role in the kinematic evolution of this region, as continent-continent collision to the NW contrasted with the Makran subduction zone in the SE (Figures 1b and 1c). The resulting gradient in the slab pull force exerted on the Arabian plate resulted in rotational anticlockwise motion of Arabia with respect to Africa, which is considered to be the main driver for the opening of the Red Sea [*Bellahsen et al.*, 2003; *Bosworth et al.*, 2005]. Estimated Cenozoic extension/compression rates, based on sea floor magnetic data, and current extension rates measured using GPS [*Chu and Gordon*, 1998; *McQuarrie et al.*, 2003; *ArRajehi et al.*, 2010; *McClusky et al.*, 2010] indicate that the rotational component of the Arabian Plate has been sustained over the last 13–14 Ma, with extension rates varying from ~7 mm/yr in the Northern Red Sea to ~16 mm/yr in the Southern Red Sea.

The effect of Afar Plume on the evolution of the Red Sea is not well understood, but it is commonly accepted that it acted as a trigger for the opening of the Red Sea-Gulf of Aden system at ~20–30 Ma [*Zeyen et al.*, 1997; *Bellahsen et al.*, 2003; *Bosworth et al.*, 2005; *ArRajehi et al.*, 2010]. *Ebinger and Sleep* [1998] suggested a model comprising a single deep mantle plume that has been channeled along preexisting zones of thin lithosphere. Several seismic tomographic studies have also suggested that channeling of Afar Plume material to the north may have been caused by the northward motion of the Arabia Plate [e.g., *Chang et al.*, 2011; *Hansen and Nyblade*, 2013; *Rolandone et al.*, 2013]. The resulting thermal anomaly in the lithospheric mantle is hypothesized to cause significant localized weakening of the lithosphere in the Red Sea region [e.g., *Bastow et al.*, 2005; *Corti*, 2008; *Hill*, 1991; *Keranen and Klemperer*, 2008].

Despite the simplifications in our analogue models, the scenario of an Afar Plume-related linear thermal anomaly is analogous to Experiments 11 and 18 with a low obliquity linear weakness in the lithospheric mantle (Figures 11 and 12d). Although the obliquity in nature is actually closer to 30° than to 15°, based on the position of the linear weakness (i.e., southern end of the weakness closer to the point of maximum extension) and on constraints from structural and geophysical data, we selected Experiment 11 ($\alpha = 15°$) for comparison. The rotational component imposed in the models is comparable to the last extensional phase in the Red Sea-Gulf of Aden system (Figure 1c; 13 Ma–present). South to north rift propagation in these experiments was initially controlled by the underlying weakness zone. The rift propagation direction eventually changed toward the pole of rotation at later stages. This behavior resulted in a characteristic structural pattern that is similar to observations in the Red Sea-Gulf of Aden rift system. The main rift escarpments in the Ethiopian Plateau and in western Yemen are oriented approximately N-S, and the trend changes to roughly NW-SE north of latitude 16–18°N (Figure 12c). Since continental rift initiation took place under an orthogonal extension regime for the entire southern Red Sea [*Bosworth et al.*, 2005], this irregular pattern may be explained by the presence of prerift lithospheric structures or weaknesses that localized deformation [*Lyakhovsky et al.*, 2012; *Bosworth*, 2015], which is consistent with the presence of the linear weak zones imposed in our models (Figure 12d).

The subsequent deformation evolution in the southern Red Sea is strikingly similar to Experiment 11 (Figures 6 and 12d). The early stages in this experiment (Figure 6, 2.5% extension) show a compartmentalization of deformation in the vicinity of the weak lithosphere boundary zone. These compartments are analogous to the two rift branches in the southern Red Sea, namely, a continuation of the main Red Sea Rift to the south and a western bifurcation known as the Danakil Depression (Figure 12c). Progressive stretching of the model led to the development of an intrarift block that rotates counterclockwise about an independent pole of rotation (Figure 6, >10% extension), located in the western rift boundary. This resembles the proposed "crank-arm" model evolution for the Danakil Block [*Sichler*, 1980; *Souriot and Brun*, 1992], and it is supported by recent geodetic measurements [e.g., *McClusky et al.*, 2010]. Comparison between nature and analogue models suggest that differences in the rheological layering in the lithosphere, potentially caused by a channeling of the Afar Plume underneath the Arabian Plate, may have caused the formation of the Danakil Block (Figures 12c and 12d). Our models also suggest that extremely thinned sections of the

lithosphere gave rise to mantle exhumation, which occurs in the center of the model and then extends north and south at later stages (Figure 10b). Although our models cannot reproduce the full transition from continental break up to ocean initiation and seafloor spreading, the results are comparable with nature as crustal rupture is the final stage before the accretion of new oceanic crust, as has been occurring in the southern Red Sea since the Miocene-Pliocene transition (~5 Ma) [*Bosworth et al.*, 2005].

5. Conclusions

Three-dimensional analogue models of rotational extension provide insights on how continental rifts interact with linear heterogeneities contained in the lithospheric mantle as they propagate toward a pole of rotation. The models allowed us to characterize the evolution of deformation as a function of the orientation of linear weaknesses with respect to the initial direction of extension. The results suggest that a weakness that is close in orientation to the rift axis (i.e., low obliquity) produces strain localization in short, narrow compartments at early stages which then merge and propagate at regular rates by a process of unzipping. In these scenarios, the displacement gradient along the rift axis caused by the rotational boundary condition may contribute to the formation of rotating intrarift horsts. Models with a weakness that is unfavorably oriented to the rift axis (i.e., moderate/high obliquity) show strong partitioning of deformation. Large-scale V-shaped extensional basins that are synchronously abandoned can be explained by conditions similar to those replicated in these experiments.

By incorporating a rotating stretching vector in our analogue models, we conclude that even short periods (model: ~12 h; nature: <10 Ma) of continuous change in the extension direction can produce first-order structures that will govern the overall rift architecture. These changes in plate kinematics may also impact directly on the time and location of ocean initiation. When a linear lithospheric mantle weakness is present, it exerts a first-order control on the onset of mantle exhumation and potentially on the location of subsequent seafloor spreading centers.

References

Adam, J., J. L. Urai, B. Wienecke, O. Oncken, K. Pfeiffer, N. Kukowski, J. Lohrmann, S. Hoth, W. van der Zee, and J. Schmatz (2005), Shear localisation and strain distribution during tectonic faulting—New insights from granular-flow experiments and high-resolution optical image correlation techniques, *J. Struct. Geol.*, *27*(2), 283–301, doi:10.1016/j.jsg.2004.08.008.

Agostini, A., G. Corti, A. Zeoli, and G. Mulugeta (2009), Evolution, pattern, and partitioning of deformation during oblique continental rifting: Inferences from lithospheric-scale centrifuge models, *Geochem. Geophys. Geosyst.*, *10*, Q11015, doi:10.1029/2009GC002676.

Almalki, K. A., P. G. Betts, and L. Ailleres (2015), The Red Sea—50 years of geological and geophysical research, *Earth Sci. Rev.*, doi:10.1016/j.earscirev.2015.05.002.

ArRajehi, A., et al. (2010), Geodetic constraints on present-day motion of the Arabian Plate: Implications for Red Sea and Gulf of Aden rifting, *Tectonics*, *29*, TC3011, doi:10.1029/2009TC002482.

Artyushkov, E. V. (1983), *Geodynamics*, pp. 312, Elsevier, Amsterdam.

Autin, J., N. Bellahsen, L. Husson, M. Beslier, S. Leroy, and E. D'Acremont (2010), Analog models of oblique rifting in a cold lithosphere, *Tectonics*, *29*, TC6016, doi:10.1029/2010TC002671.

Bastow, I. D., G. W. Stuart, J. M. Kendall, and C. J. Ebinger (2005), Upper-mantle seismic structure in a region of incipient continental breakup: Northern Ethiopian rift, *Geophys. J. Int.*, *162*(2), 479–493, doi:10.1111/j.1365-246X.2005.02666.x.

Bellahsen, N., C. Faccenna, F. Funiciello, J. M. Daniel, and L. Jolivet (2003), Why did Arabia separate from Africa? Insights from 3-D laboratory experiments, *Earth Planet. Sci. Lett.*, *216*(3), 365–381, doi:10.1016/S0012-821X(03)00516-8.

Benes, V., and P. Davy (1996), Modes of continental lithospheric extension: Experimental verification of strain localization processes, *Tectonophysics*, *254*(1–2), 69–87, doi:10.1016/0040-1951(95)00076-3.

Benes, V., and S. Scott (1996), Oblique rifting in the Havre Trough and its propagation into the continental margin of New Zealand: Comparison with analogue experiments, *Mar. Geophys. Res.*, *18*(2–4), 189–201, doi:10.1007/BF00286077.

Bercovici, D., and Y. Ricard (2014), Plate tectonics, damage and inheritance, *Nature*, *508*(7497), 513–6, doi:10.1038/nature13072.

Bonatti, E., M. Seyler, J. Channell, J. Giraudeau, and G. Mascle (1990), Peridotites drilled from the Tyrrhenian Sea, ODP Leg 107, in *Proceedings of Ocean Drilling Program*, *Sci Res*, 107, edited by K. A. Kastens, et al., 37-47, College Station, Tex., doi:10.2973/odp.proc. sr.107.141.1990.

Bonini, M., T. Souriot, M. Boccaletti, and J. P. Brun (1997), Successive orthogonal and oblique extension episodes in a rift zone: Laboratory experiments with application to the Ethiopian Rift, *Tectonics*, *16*(2), 347–362, doi:10.1029/96TC03935.

Bosworth, W. (2015), Geological Evolution of the Red Sea: Historical Background, Review and Synthesis, in *The Red Sea: The formation, Morphology, Oceanography and Environment of a Young Ocean Basin*, edited by N. M. A. Rasul and I. C. F. Stewart, pp. 45–78, Springer, Berlin, doi:10.1007/978-3-662-45201-1_3.

Bosworth, W., P. Huchon, and K. McClay (2005), The Red Sea and Gulf of Aden basins, *J. Afr. Earth Sci.*, *43*(1–3), 334–378, doi:10.1016/j.jafrearsci.2005.07.020.

Boutelier, D., and A. Cruden (2013), Slab rollback rate and trench curvature controlled by arc deformation, *Geology*, *41*(8), 911–914, doi:10.1130/G34338.1.

Boutelier, D., B. Saumur, and A. R. Cruden (2016), Density and visco-elasticity of Natrosol 250 HH solutions for experimental tectonics, *J. Struct. Geol.*, 1–38, doi:10.1016/j.jsg.2016.03.001.

Brune, S. (2014), Evolution of stress and fault patterns in oblique rift systems: 3D numerical lithospheric-scale experiments from rift to breakup, *Geochem. Geophys. Geosyst.*, *15*, 3392–3415, doi:10.1002/2014GC005446.

Buttinelli, M., D. Scrocca, D. De Rita, and F. Quattrocchi (2014), Modes of stepwise eastward migration of the northern Tyrrhenian Sea back-arc extension: Evidences from the northern Latium offshore (Italy), *Tectonics*, *33*, 187–206, doi:10.1002/2013TC003365.

Byerlee, J. (1978), Friction of rocks, *Pure Appl. Geophys.*, *116*, 615–626.

Chang, S. J., M. Merino, S. Van Der Lee, S. Stein, and C. A. Stein (2011), Mantle flow beneath Arabia offset from the opening Red Sea, *Geophys. Res. Lett.*, *38*, L04301, doi:10.1029/2010GL045852.

Chen, Z., W. P. Schellart, V. Strak, and J. C. Duarte (2016), Does subduction-induced mantle flow drive backarc extension?, *Earth Planet. Sci. Lett.*, *441*, 200–210, doi:10.1016/j.epsl.2016.02.027.

Chu, D., and R. Gordon (1998), Current plate motions across the Red Sea, *Geophys. J. Int.*, *135*(2), 313–328, doi:10.1046/j.1365-246X.1998.00658.x.

Corti, G. (2008), Control of rift obliquity on the evolution and segmentation of the main Ethiopian rift, *Nat. Geosci.*, *1*(4), 258–262, doi:10.1038/ngeo160.

Corti, G., M. Bonini, S. Conticelli, F. Innocenti, P. Manetti, and D. Sokoutis (2003), Analogue modelling of continental extension: A review focused on the relations between the patterns of deformation and the presence of magma, *Earth Sci. Rev.*, *63*(3–4), 169–247, doi:10.1016/S0012-8252(03)00035-7.

Courtillot, V. E. (1982), Propagating rifts and continental breakup, *Tectonics*, *1*(3), 239–250, doi:10.1029/TC001i003p00239.

Cruden, A., M. Nasseri, and R. Pysklywec (2006), Surface topography and internal strain variation in wide hot orogens from three-dimensional analogue and two-dimensional numerical vice models, *Geol. Soc. Spec. Publ.*, *253*(1), 79–104, doi:10.1144/GSL.SP.2006.253.01.04.

Davaille, A. (1999), Two-layer thermal convection in miscible viscous fluids, *J. Fluid Mech.*, *379*, 223–253, doi:10.1017/S0022112098003322.

Davaille, A., F. Girard, and M. Le Bars (2002), How to anchor hotspots in a convecting mantle?, *Earth Planet. Sci. Lett.*, *203*(2), 621–634, doi:10.1016/S0012-821X(02)00897-X.

Davy, P., and P. Cobbold (1991), Experiments on shortening of a 4-layer model of the continental lithosphere, *Tectonophysics*, *188*, 1–25.

Ding, W., and J. Li (2016), Propagated rifting in the Southwest Sub-basin, South China Sea: Insights from analogue modelling, *J. Geodyn.*, doi:10.1016/j.jog.2016.02.004.

Dixon, T., R. Stern, and I. Hussein (1987), Control of Red Sea rift geometry by Precambrian structures, *Tectonics*, *6*(5), 551–571, doi:10.1029/TC006i005p00551.

Duarte, J., W. P. Schellart, and A. Cruden (2014), Rheology of petrolatum–paraffin oil mixtures: Applications to analogue modelling of geological processes, *J. Struct. Geol.*, *63*, 1–11, doi:10.1016/j.jsg.2014.02.004.

Dunbar, J. A., and D. S. Sawyer (1996), Three-dimensional dynamical model of continental rift propagation and margin plateau formation, *J. Geophys. Res.*, *101*(B12), 27,845–27,863, doi:10.1029/96JB01231.

Ebinger, C. J., and N. H. Sleep (1998), Cenozoic magmatism throughout east Africa resulting from impact of a single plume, *Nature*, *395*, 788–791, doi:10.1038/27417.

Faccenna, C., P. Davy, J.-P. Brun, R. Funiciello, D. Giardini, M. Mattei, and T. Nalpas (1996), The dynamics of back-arc extension: An experimental approach to the opening of the Tyrrhenian Sea, *Geophys. J. Int.*, *126*(3), 781–795, doi:10.1111/j.1365-246X.1996.tb04702.x.

Faccenna, C., M. Mattei, R. Funiciello, and L. Jolivet (1997), Styles of back-arc extension in the Central Mediterranean, *Terra Nova*, *9*(3), 126–130, doi:10.1046/j.1365-3121.1997.d01-12.x.

Finetti, I. (1982), Structure, stratigraphy and evolution of Central Mediterranean, *Boll. Geof. Teor. Appl.*, *24*, 247–314.

Fournier, M., and C. Petit (2007), Oblique rifting at oceanic ridges: Relationship between spreading and stretching directions from earthquake focal mechanisms, *J. Struct. Geol.*, *29*(2), 201–208, doi:10.1016/j.jsg.2006.07.017.

Fournier, M., N. Bellahsen, O. Fabbri, and Y. Gunnell (2004), Oblique rifting and segmentation of the NE Gulf of Aden passive margin, *Geochem. Geophys. Geosyst.*, *5*, Q11005, doi:10.1029/2004GC000731.

Funiciello, F., C. Faccenna, A. Heuret, S. Lallemand, E. Di Giuseppe, and T. W. Becker (2008), Trench migration, net rotation and slab-mantle coupling, *Earth Planet. Sci. Lett.*, *271*(1–4), 233–240, doi:10.1016/j.epsl.2008.04.006.

Hansen, S. E., and A. A. Nyblade (2013), The deep seismic structure of the Ethiopia/Afar hotspot and the African superplume, *Geophys. J. Int.*, *194*(1), 118–124, doi:10.1093/gji/ggt116.

Heron, P. J., R. N. Pysklywec, and R. Stephenson (2016), Lasting mantle scars lead to perennial plate tectonics, *Nat. Commun.*, *7*, 11,834, doi:10.1038/ncomms11834.

Hey, R. (1977), A new class of "pseudofaults" and their bearing on plate tectonics: A propagating rift model, *Earth Planet. Sci. Lett.*, *37*, 321–325.

Hey, R., F. K. Duennebier, and W. J. Morgan (1980), Propagating rifts on midocean ridges, *J. Geophys. Res.*, *85*(B7), 3647–3658, doi:10.1029/JB085iB07p03647.

Hey, R., F. Martinez, Á. Höskuldsson, and Á. Benediktsdóttir (2010), Propagating rift model for the V-shaped ridges south of Iceland, *Geochem. Geophys. Geosyst.*, *11*, Q03011, doi:10.1029/2009GC002865.

Hill, R. I. (1991), Starting plumes and continental break-up, *Earth Planet. Sci. Lett.*, *104*, 398–416, doi:10.1016/0012-821X(91)90218-7.

Huismans, R., and C. Beaumont (2014), Rifted continental margins: The case for depth-dependent extension, *Earth Planet. Sci. Lett.*, *407*, 148–162, doi:10.1016/j.epsl.2014.09.032.

Kastens, K. A., et al. (1987), *Proceedings of the Ocean Drilling Program (Part A—Initial Reports, Sites 650–656)*, vol. 107, pp. 772, Ocean Drilling Program, College Station, Tex.

Kastens, K., J. Mascle, and O.D.P Scientific Party (1988), ODP leg 107 in the Tyrrhenian Sea: Insights into passive margin and back-arc basin evolution, *Geol. Soc. Am. Bull.*, *100*, 1140–1156.

Kazmin, V., A. S. Shifferaw, and T. Balcha (1978), The Ethiopian basement: Stratigraphy and possible manner of evolution, *Geol. Rundsch.*, *67*, 531–546.

Keep, M., and K. R. McClay (1997), Analogue modelling of multiphase rift systems, *Tectonophysics*, *273*(3–4), 239–270, doi:10.1016/S0040-1951(96)00272-7.

Keranen, K., and S. L. Klemperer (2008), Discontinuous and diachronous evolution of the Main Ethiopian Rift: Implications for development of continental rifts, *Earth Planet. Sci. Lett.*, *265*(1–2), 96–111, doi:10.1016/j.epsl.2007.09.038.

Lyakhovsky, V., A. Segev, U. Schattner, and R. Weinberger (2012), Deformation and seismicity associated with continental rift zones propagating toward continental margins, *Geochem. Geophys. Geosyst.*, *13*, Q01012, doi:10.1029/2011GC003927.

Malinverno, A., and W. B. F. Ryan (1986), Extension in the Tyrrhenian Sea and shortening in the Apennines as result of arc migration driven by sinking of the lithosphere, *Tectonics*, *5*(2), 227–245, doi:10.1029/TC005i002p00227.

Manatschal, G., L. Lavier, and P. Chenin (2015), The role of inheritance in structuring hyperextended rift systems: Some considerations based on observations and numerical modeling, *Gondwana Res.*, *27*(1), 140–164, doi:10.1016/j.gr.2014.08.006.

Marques, F., P. Cobbold, and N. Lourenço (2007), Physical models of rifting and transform faulting, due to ridge push in a wedge-shaped oceanic lithosphere, *Tectonophysics*, *443*(1–2), 37–52, doi:10.1016/j.tecto.2007.07.002.

Mart, Y., and O. Dauteuil (2000), Analogue experiments of propagation of oblique rifts, *Tectonophysics*, *316*, 121–132.

Martin, A. K. (1984), Propagating rifts: Crustal extension during continental rifting, *Tectonics*, *3*(6), 611–617, doi:10.1029/TC003i006p00611.

Mattei, M., C. Kissel, and R. Funiciello (1996), No tectonic rotation of the Tuscan Tyrrhenian margin (Italy) since late Messinian, *J. Geophys. Res.*, *101*(2), 2835–2845, doi:10.1029/95JB02398.

McClusky, S., et al. (2010), Kinematics of the southern Red Sea-Afar Triple Junction and implications for plate dynamics, *Geophys. Res. Lett.*, *37*, L05301, doi:10.1029/2009GL041127.

McQuarrie, N., J. M. Stock, C. Verdel, and B. P. Wernicke (2003), Cenozoic evolution of Neotethys and implications for the causes of plate motions, *Geophys. Res. Lett.*, *30*(20), 2036, doi:10.1029/2003GL017992.

Milia, A., and M. M. Torrente (2015), Tectono-stratigraphic signature of a rapid multistage subsiding rift basin in the Tyrrhenian-Apennine hinge zone (Italy): A possible interaction of upper plate with subducting slab, *J. Geodyn.*, *86*, 42–60, doi:10.1016/j.jog.2015.02.005.

Milia, A., M. M. Torrente, B. Massa, and P. Iannace (2013), Progressive changes in rifting directions in the Campania margin (Italy): New constrains for the Tyrrhenian Sea opening, *Global Planet. Change*, *109*, 3–17, doi:10.1016/j.gloplacha.2013.07.003.

Milia, A., M. M. Torrente, and M. Tesauro (2016), From stretching to mantle exhumation in a triangular backarc basin (Vavilov basin, Tyrrhenian Sea, Western Mediterranean), *Tectonophysics*, doi:10.1016/j.tecto.2016.10.017.

Müller, R. D., et al. (2016), Ocean basin evolution and global-scale reorganization events since Pangea breakup, *Annu. Rev. Earth Planet. Sci. Lett.*, *44*, 107–138, doi:10.1146/annurev-earth-060115-012211.

Patacca, E., R. Sartori, and P. Scandone (1990), Tyrrhenian basin and Apenninic Arcs: Kinematic relations since Late Tortonian times, *Mem. Soc. Geol. It*, *45*, 425–451, doi:10.1007/978-94-011-2016-6_7.

Philippon, M., J. P. Brun, F. Gueydan, and D. Sokoutis (2014), The interaction between Aegean back-arc extension and Anatolia escape since Middle Miocene, *Tectonophysics*, *631*(C), 176–188, doi:10.1016/j.tecto.2014.04.039.

Pysklywec, R., and A. Cruden (2004), Coupled crust-mantle dynamics and intraplate tectonics: Two-dimensional numerical and three-dimensional analogue modeling, *Geochem. Geophys. Geosyst.*, *5*, Q10003, doi:10.1029/2004GC000748.

Ramberg, H. (1967), Model experimentation of the effect of gravity on tectonic processes, *Geophys. J. R. Astron. Soc.*, *14*(1–4), 307–329, doi:10.1111/j.1365-246X.1967.tb06247.x.

Ranalli, G. (1995), *Rheology of the Earth*, Chapman and Hall, London.

Riller, U., A. R. Cruden, D. Boutelier, and C. E. Schrank (2012), The causes of sinuous crustal-scale deformation patterns in hot orogens: Evidence from scaled analogue experiments and the southern Central Andes, *J. Struct. Geol.*, *37*, 65–74, doi:10.1016/j.jsg.2012.02.002.

Ritsema, J., H. J. Van Heijst, and J. H. Woodhouse (1999), Complex shear wave velocity structure imaged beneath Africa and Iceland, *Science*, *286*(5446), 1925–1928, doi:10.1126/science.286.5446.1925.

Robin, C., P. Colantoni, M. Gennesseaux, and J. P. Rehault (1987), Vavilov seamount: A mildly alkaline Quaternary volcano in the Tyrrhenian Basin, *Mar. Geol.*, *78*(1–2), 125–136, doi:10.1016/0025-3227(87)90071-5.

Rolandone, F., F. Lucazeau, S. Leroy, J. C. Mareschal, R. Jorand, B. Goutorbe, and H. Bouquerel (2013), New heat flow measurements in Oman and the thermal state of the Arabian Shield and Platform, *Tectonophysics*, *589*, 77–89, doi:10.1016/j.tecto.2012.12.034.

Rosenbaum, G., and G. S. Lister (2004), Neogene and Quaternary rollback evolution of the Tyrrhenian Sea, the Apennines, and the Sicilian Maghrebides, *Tectonics*, *23*, TC1013, doi:10.1029/2003TC001518.

Schellart, W. P. (2000), Shear test results for cohesion and friction coefficients for different granular materials: Scaling implications for their usage in analogue modelling, *Tectonophysics*, *324*(1–2), 1–16, doi:10.1016/S0040-1951(00)00111-6.

Schellart, W. P. (2008), Kinematics and flow patterns in deep mantle and upper mantle subduction models: Influence of the mantle depth and slab to mantle viscosity ratio, *Geochem. Geophys. Geosyst.*, *9*, Q03014, doi:10.1029/2007GC001656.

Schellart, W. P., M. Jessell, and G. Lister (2003), Asymmetric deformation in the backarc region of the Kuril arc, northwest Pacific: New insights from analogue modeling, *Tectonics*, *22*(5), 1047, doi:10.1029/2002TC001473.

Schrank, C. E., D. A. Boutelier, and A. R. Cruden (2008), The analogue shear zone: From rheology to associated geometry, *J. Struct. Geol.*, *30*(2), 177–193, doi:10.1016/j.jsg.2007.11.002.

Sella, G. F., T. H. Dixon, and A. Mao (2002), REVEL: A model for recent plate velocities from space geodesy, *J. Geophys. Res.*, *107*(B4), 2081, doi:10.1029/2000JB000033.

Seton, M., et al. (2012), Global continental and ocean basin reconstructions since 200 Ma, *Earth Sci. Rev.*, *113*(3–4), 212–270, doi:10.1016/j.earscirev.2012.03.002.

Shih, J., and P. Molnar (1975), Analysis and implications of the sequence of ridge jumps that eliminated the Surveyor Transform Fault, *J. Geophys. Res.*, *80*(35), 4815–4822, doi:10.1029/JB080i035p04815.

Sichler, B. (1980), La biellette danakile : Un modèle pour l'évolution géodynamique de l'Afar, *Bull. Soc. Géol. Fr.*, *22*(701), 925–933.

Souriot, T., and J. P. Brun (1992), Faulting and block rotation in the Afar triangle, East Africa: The Danakil "crank-arm" model, *Geology*, *20*(10), 911–914, doi:10.1130/0091-7613(1992)020<0911:FABRIT>2.3.CO;2.

Sun, Z., Z. Zhong, M. Keep, D. Zhou, D. Cai, X. Li, S. Wu, and J. Jiang (2009), 3D analogue modeling of the South China Sea: A discussion on breakup pattern, *J. Asian Earth Sci.*, *34*(4), 544–556, doi:10.1016/j.jseaes.2008.09.002.

Tommasi, A., and A. Vauchez (2001), Continental rifting parallel to ancient collisional belts: An effect of the mechanical anisotropy of the lithospheric mantle, *Earth Planet. Sci. Lett.*, *185*(1–2), 199–210, doi:10.1016/S0012-821X(00)00350-2.

Tron, V., and J. P. Brun (1991), Experiments on oblique rifting in brittle-ductile systems, *Tectonophysics*, *188*, 71–84, doi:10.1016/0040-1951(91)90315-J.

van Wijk, J. (2005), Role of weak zone orientation in continental lithosphere extension, *Geophys. Res. Lett.*, *32*, L02303, doi:10.1029/2004GL022192.

van Wijk, J. W., and D. K. Blackman (2005), Dynamics of continental rift propagation: The end-member modes, *Earth Planet. Sci. Lett.*, *229*(3–4), 247–258, doi:10.1016/j.epsl.2004.10.039.

Wilson, T. (1966), Did the Atlantic close and then re-open?, *Nature*, *211*, 676–681.

Wu, B., C. P. Conrad, A. Heuret, C. Lithgow-Bertelloni, and S. Lallemand (2008), Reconciling strong slab pull and weak plate bending: The plate motion constraint on the strength of mantle slabs, *Earth Planet. Sci. Lett.*, *272*(1–2), 412–421, doi:10.1016/j.epsl.2008.05.009.

Zeyen, H., F. Volker, V. Wehrle, K. Fuchs, S. Sobolev, and R. Altherr (1997), Styles of continental rifting: Crust-mantle detachment and mantle plumes, *Tectonophysics*, *278*(1–4), 329–352, doi:10.1016/S0040-1951(97)00111-X.

Zwaan, F., G. Schreurs, J. Naliboff, and S. H. Buiter (2016), Insights into the effects of oblique extension on continental rift interaction from 3D analogue and numerical models, *Tectonophysics*, doi:10.1016/j.tecto.2016.02.036.